



Vertical structure and microphysical observations of winter precipitation in an inner valley during the Cerdanya-2017 field campaign

Sergi González ^{a,b,*}, Joan Bech ^b, Albert Garcia-Benadí ^{b,c}, Mireia Udina ^b, Bernat Codina ^b, Laura Trapero ^d, Alexandre Paci ^e, Jean-François Georgis ^f

^a DT Catalonia, Agencia Estatal de Meteorología (AEMET), Barcelona, Spain

^b Department of Applied Physics - Meteorology, University of Barcelona, Barcelona, Spain

^c SARTI, Universitat Politècnica de Catalunya, Vilanova i la Geltrú, Spain

^d Snow and Mountain Research Center of Andorra (CENMA-IEA), Andorra Research Institute, Andorra

^e Centre National de Recherches Météorologiques (CNRM), Université de Toulouse, MÉTEO-FRANCE, CNRS, Toulouse, France

^f Laboratoire d'Aérologie, Université de Toulouse, CNRS, Toulouse, France

ARTICLE INFO

Keywords:

Mountain precipitation

Inner valley

Micro Rain Radar

Parsivel disdrometer

Microphysical processes

Pyrenees

Cerdanya-2017

ABSTRACT

Precipitation processes at windward and leeward sides of the mountains have been object of study for many decades. Instead, inner mountain valleys, where usually most mountain population lives, have received considerably less attention. This article examines precipitation processes during a winter field campaign in an inner valley of the Pyrenees (NE Spain) using, among other instruments, a K-band vertically pointing Doppler radar (Micro Rain Radar) and a laser-based optical disdrometer (Parsivel). A decoupling is found between the stalled air of the valley and the air of the free atmosphere above the mountain crest level, evidenced by an increase of turbulence and spectral width of precipitation particles. Wind shear layer may promote riming and aggregation of the ice and snow particles. Two main rainfall regimes are found during the campaign: (1) stratiform rainfall mostly produced by water vapour deposition processes, although sometimes riming and aggregation become important, and (2) weak convection with slight dominance of collision-coalescence processes. Precipitation characteristics at the bottom of the valley show typical continental features such as low Liquid Water Content, despite the valley is only about 100 km from the sea. This study demonstrates that inner valley may present distinct precipitation features with respect to windward and leeward precipitation.

1. Introduction

Orographic interaction with precipitating clouds depends on multiple factors (Houze, 2012; Roe, 2005). Static stability, moisture content or vertical profile and strength of the air flow affect orographic precipitation (Medina et al., 2005). The specific geometry of the air flow orientation with respect to terrain is also very important (Roe, 2005). Those interactions are commonly explained from the point of view of the windward vs. leeward duality. In the simplest conceptual idealized model, precipitation is enhanced by forced ascent on the windward side of a two-dimensional mountain and appears a precipitation shadow on the leeside where air sinks. Further investigations have demonstrated that interactions between air flow and precipitation can be much more complex. Several mesoscale and microscale processes modify the precipitation growth, intensity, distribution and phase (Aikins et al., 2016;

Garvert et al., 2007; Geerts et al., 2011; Houze et al., 2017; Medina and Houze, 2003). An example is the presence of a persistent wind shear layer observed upstream of major mountain ranges in stable stratified low-level flow (Medina et al., 2005; Medina and Houze, 2015). This layer increases turbulence, which has been observed to enhance the precipitation over the windward slopes. Another notable example of orographic complexity is caused by the forced updrafts that trigger shallow convective systems (Konwar et al., 2014; Murata et al., 2020), where the process of coalescence produces a large number of relatively small raindrops. This process is fundamental to produce high amounts of orographic precipitation in areas such as the Western Ghats of India (Das et al., 2017; Konwar et al., 2014) or Cherrapunji (Murata et al., 2020). Note that the latter location holds the world record for rainfall amounts at several temporal durations between two days and two years (Galmariini et al., 2004; Gonzalez and Bech, 2017).

* Corresponding author at: DT Catalonia, AEMET. C/ Arquitecte Sert, 1, E-08003 Barcelona, Spain.

E-mail address: sgonzalezh@aemet.es (S. González).

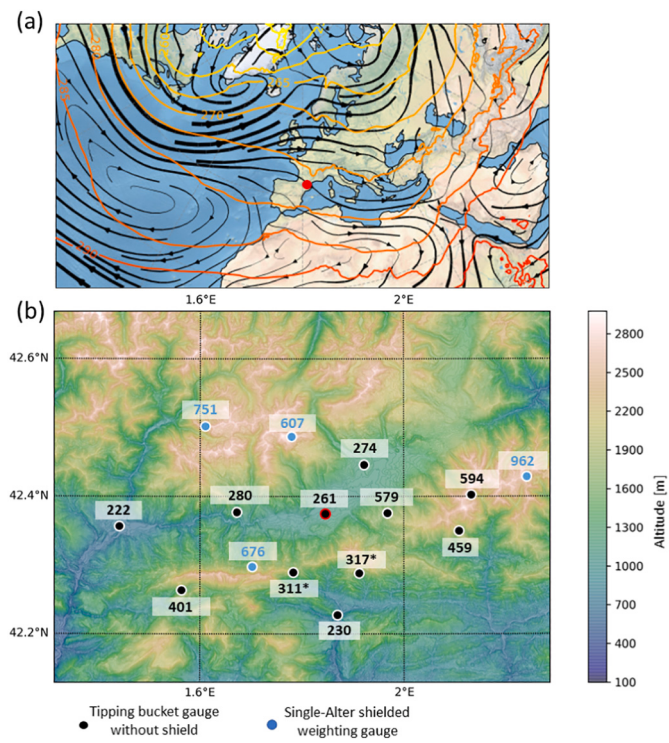


Fig. 1. (a) Location of the Cerdanya valley (red circle) at the eastern side of Pyrenees mountain massif in south-west Europe with the 850 hPa temperature (contours) and wind (streamlines proportional to the wind speed) averaged from Jan to Apr 2017 using ERA5 data. (b) Map of the Cerdanya valley showing precipitation (mm) corrected for undercatch wind effects during the C2017 field campaign recorded at single-Alter shielded weighting gauges (blue solid circles) and tipping bucket heated gauges (black solid circles). Precipitation records at gauges without collocated wind measurements (indicated by the * symbol) were not corrected. The main observing site is located at LECD aerodrome (black circle with red contour; 260.9 mm, 1097 m *asl*). Malniu (606.7, 2230 m *asl*) is located at the north-northwest of LECD. (For interpretation of the references to colour in this figure legend, the reader is referred to the web version of this article.)

Many mountain systems have several regions that cannot be described using the simple windward or leeward model (Prat and Barros, 2010). This is the case of inner valleys, characterized by being surrounded by other valleys with different orientations, which produces a relative isolation with respect to the synoptic wind flow. Inner valleys have received considerably less attention than windward and leeward slopes. As far as we know, only Prat and Barros (2010) have focused on the characterization of precipitation processes of inner regions, studied in the mountains in the Great Smoky Mountains in the Southern Appalachians. Additionally, other precipitation studies have been performed on inner valleys, specifically at the Tropical Andes (Kumar et al., 2020; Seidel et al., 2019). Inner valleys present an additional challenge to the study of the precipitation processes: conventional ground-based weather radars become blocked by the surrounding mountains preventing low-level in-valley measurements (Bech et al., 2007; Bech et al., 2003; Prat and Barros, 2010; Trapero et al., 2009). In addition, spaceborne radar precipitation estimates from satellites such as the Core Observatory satellite of the Global Precipitation Measurement (GPM) mission are affected by ground clutter hampering near-ground measurements (Maahn et al., 2014) and this cluttering may be even worse in valleys due to the proximity of mountain slopes (Arulraj and Barros, 2021). Because of these limitations, ground-based vertical-profiling radars –able to provide high temporal (1 min) and vertical spatial (100 m) resolutions– become a suitable tool to study precipitation in inner valleys together with in-situ precipitation measurements such as rain-

gauges and disdrometers.

The main scientific objective of this paper is to present an analysis of winter precipitation observations measured in an inner valley, studying their vertical variability and dominant microphysical processes in order to expand the current limited literature on the topic. In particular, we want to assess if the isolation of an inner valley in the Pyrenees Mountains may lead to more continental conditions than expected given the proximity to the Mediterranean Sea. For this purpose, we carried out a field campaign at the Cerdanya Valley in the eastern Pyrenees from December 2016 to April 2017. A dedicated network of non-conventional meteorological instrumentation was deployed including, among others, a Micro-Rain Radar and a Parsivel disdrometer. A description of the area of interest is presented in Section 2 and the instrumentation used in this study is described in Section 3. Section 4 presents the results of the campaign describing the precipitation events (Section 4.1), the vertical profiles during the snowfall events (Section 4.2), the drop size distribution of the rainfall events (Section 4.3), and the analysis of two selected case studies (Section 5). Main conclusions and outlook for future work are described in Section 6.

2. Region of study

The Pyrenees mountain massif is an important ecoregion in southwestern Europe with a high level of biodiversity and endemic species. From the human perspective, it is a strategic region for energy production (López-Moreno et al., 2002), tourism (Lasanta et al., 2007) and water management in north-eastern Spain (López-Moreno et al., 2014). Precipitation is therefore an essential resource in this area that has been extensively investigated from the climatic point of view (Buisan et al., 2015; Lemus-Canovas et al., 2019; Pérez-Zanón et al., 2017) and mesoscale factors associated to heavy rainfall events (Trapero et al., 2013a, 2013b).

Located on the Eastern Pyrenees, the Cerdanya is a wide inner valley (~15 km at the minor axis and 35 km at the major axis) corresponding to the higher basin of the Segre River, a tributary of the Ebro river basin (Fig. 1). Unlike most valleys of the Pyrenees with N-S orientation, the Cerdanya is oriented from east-northeast to west-southwest. The bottom of the valley, where most instruments were located is at 1100 m above sea level (*asl*). The valley narrows to the west-southwest and is surrounded by mountain ranges at northwest and southeast with mountain peaks exceeding 2000 m *asl*. Therefore it is a quite enclosed valley. Several small valleys drain to the wide Cerdanya valley in addition to the surrounding slopes causing frequent thermal inversions in the bottom of the valley in winter (Conangla et al., 2018; Miró et al., 2018; Pagès et al., 2017).

The Cerdanya valley has a large precipitation gradient with altitude. The lowest inner areas of the valley have yearly averages about 600 mm yr^{-1} while in the surrounding mountains the precipitation may exceed 1400 mm yr^{-1} (Xercavins, 1985), thus presenting a classical rain shadow pattern. Unlike other neighbouring Mediterranean areas, the summer in the Cerdanya valley is the wet season and winter is historically considered the dry season. However, this climatology may be biased due to underestimation of solid precipitation in rain gauges as described in previous studies (Buisán et al., 2017; Rasmussen et al., 2012). Snow days show a great dependence with altitude. In the inner valley, there are less than 20 days of snow a year while there are more than 40 days of snow a year in the surrounding mountains, especially in the northern mountains more exposed to the winter northerlies (Xercavins, 1985).

3. Instrumentation and methodology

From December 2017 to May 2017, a field campaign was conducted to study cold pools, mountain waves, rotors and precipitation in this mountainous terrain area (see f.e. Gonzalez et al., 2019; Udina et al., 2020). During the campaign, named Cerdanya-2017 (hereafter C2017),

Table 1

Precipitation events observed during the C2017, indicating the date and time of the event, the duration, type of hydrometeor on surface (snow, mixed, rain or virga), depth of the precipitation column over 10 dBZ (Shallow: < 2500 m, Borderline: 2500–3000 m, Tall: >3000 m), continuity of the precipitation into the event and availability of Parsivel measurements (A: available; NA: not available; P: partially available).

Event	Year	Month	Start day	Start time	End day	End time	Duration (h)	Type	Depth	Continuity	Parsivel
1	2017	1	10	10:30	10	13:30	3	Snow to Mixed	Tall - Borderline-Shallow	Continuous	A
2	2017	1	10	19:00	11	1:00	6	Snow	Borderline -Shallow	Continuous	A
3	2017	1	13	3:00	13	18:00	15	Virga-Snow	Borderline - Shallow	Scattered	A
4	2017	1	14	2:00	14	22:00	10	Virga-Snow	Borderline -Shallow	Scattered	A
5 ^a	2017	1	14	22:00	16	15:00	41	Snow	Tall -Borderline	Continuous	A
6	2017	1	25	14:00	26	15:00	25	Snow	Tall -Shallow	Scattered	NA
7	2017	1	27	7:00	28	6:00	23	Snow	Tall - Borderline	Continuous	NA
8	2017	1	28	17:00	28	20:00	3	Virga	Borderline	Isolated	NA
9	2017	2	2	7:00	2	20:00	13	Rain	Tall - Shallow	Scattered	NA
10	2017	2	3	8:00	3	13:00	5	Snow to Mixed	Tall - Shallow	Scattered	NA
11	2017	2	3	20:00	4	8:00	12	Snow to Rain	Shallow	Scattered	NA
12	2017	2	4	15:00	5	11:00	20	Rain	Shallow - Borderline - Tall	Scattered	NA
13	2017	2	5	13:00	6	7:00	18	Snow	Tall - Borderline	Continuous	NA
14	2017	2	6	17:00	7	0:00	7	Rain	Shallow	Continuous	NA
15	2017	2	7	18:00	8	1:00	7	Rain or Mixed	Tall -Borderline	Scattered	NA
16	2017	2	8	3:00	8	6:00	3	Virga	Tall	Isolated	NA
17	2017	2	11	14:00	12	3:00	13	Rain or Mixed	Borderline	Scattered	NA
18	2017	2	12	13:00	12	15:00	2	Virga	Borderline	Isolated	NA
19	2017	2	12	19:00	14	7:00	36	Rain or Mixed	Tall-Borderline-Shallow	Scattered	NA
20	2017	2	24	2:00	24	3:00	1	Rain	Borderline	Isolated	NA
21	2017	2	28	17:00	28	19:00	2	Probably Mixed	Tall	Isolated	NA
22	2017	3	3	18:00	4	4:00	10	Rain to Mixed	Tall	Continuous	NA
23	2017	3	4	16:30	4	18:00	1.5	Snow	Tall	Isolated	NA
24 ^b	2017	3	6	5:00	6	10:00	5	Rain	Borderline	Scattered	NA
25	2017	3	7	15:00	7	20:00	5	Rain	Borderline	Scattered	NA
26	2017	3	8	2:00	8	5:00	3	Virga	Shallow	Scattered	NA
27	2017	3	12	2:00	12	22:30	10.5	Rain and Virga	Tall	Scattered	NA
28	2017	3	22	22:00	23	12:00	14	Rain Mixed and Snow	Tall - Borderline	Scattered	A
29	2017	3	24	8:00	25	18:00	34	Rain Mixed and Snow	Tall-Borderline-Shallow	Scattered	A
30	2017	3	27	12:00	27	21:00	9	Rain	Borderline-Tall	Scattered	NA
31	2017	3	31	10:00	31	14:00	4	Virga	Tall	Scattered	NA
32	2017	3	31	18:00	31	21:00	3	Rain	Tall	–	NA
33	2017	4	1	2:00	2	1:00	23	Virga	Tall-Shallow	Scattered	NA
34	2017	4	5	18:00	5	21:00	3	Rain-Shower	Borderline - Shallow	–	NA
35	2017	4	8	17:00	8	18:00	1	Rain-Shower	Tall	Isolated	NA
36	2017	4	9	14:00	9	15:00	1	Rain-Shower	Tall	Isolated	NA
37	2017	4	13	17:00	13	18:00	1	Rain-Shower	Tall	Isolated	NA
38	2017	4	14	15:00	14	20:00	5	Virga	Tall	Scattered	NA
39	2017	4	15	13:00	15	16:00	3	Rain	Tall	Continuous	NA
40	2017	4	23	16:00	23	19:00	3	Rain	Tall	Scattered	NA
41	2017	4	25	5:00	27	16:00	59	Rain to Snow	Tall-Borderline	Scattered	P
42 ^b	2017	4	30	3:00	30	23:00	20	Rain	Tall-Borderline-Shallow	Scattered	A

^a Examined in Gonzalez et al. (2019).

^b Examined in this study.

different instrumentation was deployed including Automatic Weather Stations (AWSs), located throughout the valley, and other instruments located at Das aerodrome (ICAO code: LECD; coordinates: 42.386° N 1.867° E at 1097 m asl). The following precipitation specific instruments were installed in the C2017 field campaign.

3.1. Rain Gauges

The campaign took advantage of the previous AWSs managed by the official meteorological services that operates in the area: the Spanish Meteorological Service (AEMET), the Catalan Meteorological Service (SMC), the Andorran Study Institute (IEA) and the French Meteorological Service (METEO-FRANCE). An additional network of AWS managed by the CNRM observation group (CNRM/GMEI) was also deployed. There were rain gauges of two different kinds in the area: tipping-bucket gauges and weighting gauges. Rain gauges may have several sources of error, including systematic ones like wind deviation, wetting, evaporation and splashing (WMO, 2014). These errors are expected to be relatively small, generally less than 10% for liquid precipitation (WMO, 1994) and measure is considered without corrections. However, the same is not true with solid precipitation, when the error may achieve 80%, especially when the wind is strong (Kochendorfer et al., 2017a,

2017b; Rasmussen et al., 2012). When solid precipitation occurred, measures were corrected using the transference functions developed by Buisán et al. (2017) for unshielded tipping-bucket gauges, and by Kochendorfer et al. (2017a, 2017b) for single-Alter-shielded weighting gauges.

3.2. Parsivel disdrometer

Particle Size Velocity (Parsivel; Löffler-Mang and Joss, 2000) manufactured by OTT, Germany, is an optical laser disdrometer based on the attenuation of a laser beam obscured by falling precipitation particles. From the reduction of the output voltage and the signal duration, Parsivel determines the particle size and velocity assuming that particles are raindrop spheroids. Parsivel classifies hydrometeors in 32 diameter bins and 32 velocity bins, obtaining a matrix with the quantity of particles measured for each of the $32 \times 32 = 1024$ bins every 60 s as it was configured during this campaign. The disdrometer used during the C2017 was a first generation Parsivel. The main limitation of this instrument is the underestimation of small-size drops that presents (Wen et al., 2017). To minimize this effect, liquid precipitation measured by the disdrometer was corrected following the methodology described by Raupach and Berne (2015) and, additionally, rainfall rates below 0.2

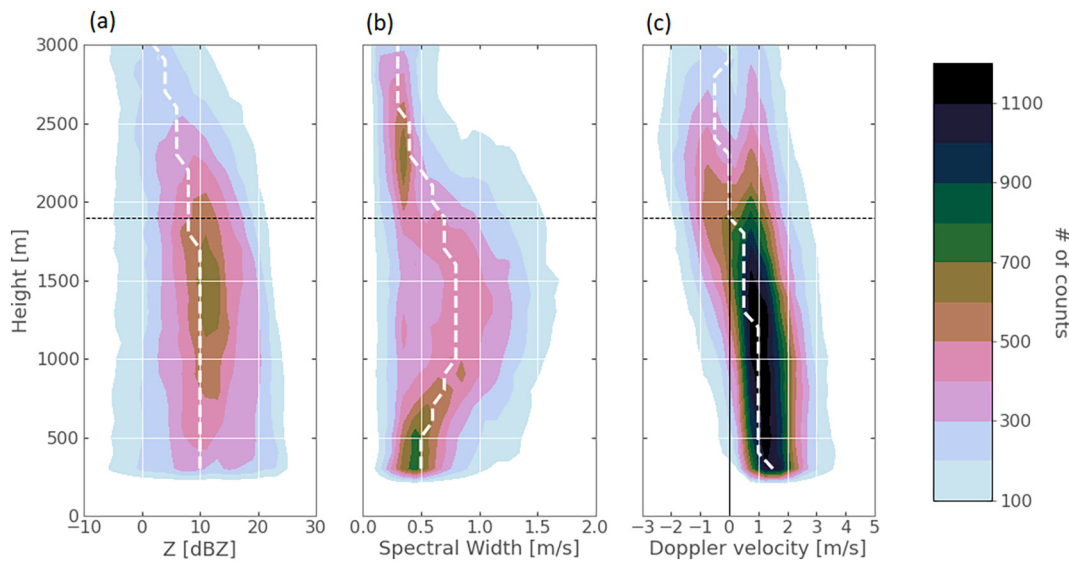


Fig. 2. (a) Radar reflectivity, (b) spectral width and (c) Doppler velocity vs. height (*agl*) measured by the MRR during snowfall events in the C2017. The white dashed line represents the median and the horizontal black line indicates the mountain top height.

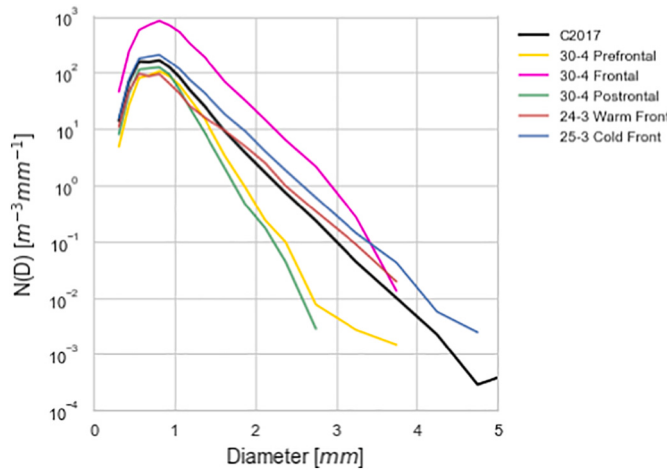


Fig. 3. DSD of liquid precipitation during the C2017 (black) and selected periods of the campaign measured by Parsivel.

Table 2

Median, standard deviation and percentiles of raindrop size distribution parameters of the rainfall precipitation during the C2017 derived from Parsivel measurements.

	D_m (mm)	$\text{Log}(N_w)$ (mm ⁻¹ m ⁻³)	LWC (g m ⁻³)	R (mm h ⁻¹)	Z (dBZ)	λ (mm ⁻¹)	μ
Mean	1.17	3.64	0.090	3.2	21.7	15.2	10.9
Std	0.35	3.70	0.120	4.3	8.2	14.7	10.9
min	0.56	0.77	0.006	0.2	3.5	1.2	-2.4
25%	0.94	3.01	0.012	0.4	14.6	5.9	3.8
50%	1.12	3.38	0.038	1.3	21.7	10.5	7.8
75%	1.35	3.77	0.125	4.3	28.6	19.1	14.4
MAX	5.23	4.52	1.303	45.2	43.1	173.7	122.0

mm h^{-1} were filtered to avoid spurious measurements. Other limitations are splashing or wind effects that also affects to other precipitation instruments. In this article, we used Parsivel to characterize the precipitation phase and the Drop Size Distribution (DSD) of the rainfall events using the manufacturer algorithm. The total number of Parsivel records

available between January and April 2017 was 51,093 min, of which 1760 min corresponded to liquid precipitation.

3.3. Micro Rain Radar

Micro Rain Radar (MRR; Peters et al., 2005) manufactured by Metek, Germany, is a portable meteorological Doppler radar profiler that operates using a FMCW (Frequency Modulated Continuous Wave) scheme in K-band (24.230 GHz). MRR operates transmitting a microwave signal and measuring the backscattered radiation by the falling particles every 10 s. The Doppler spectra is divided in 32 height bins. During the C2017 campaign, the MRR was configured to obtain 60-s averages with a height bins resolution of 100 m. To improve the sensibility of light precipitation and snow typical of winter precipitation and to avoid aliasing errors produced by ascending movements of small raindrops and snowflakes, the postprocess scheme developed by Maahn and Kollias (2012) was applied. This processing has been applied in the past to study winter and polar storms and precipitation (e.g. Durán-alarcón et al., 2018; Gonzalez et al., 2019; Gorodetskaya et al., 2015; Minder et al., 2015; Souverijns et al., 2017; Stark et al., 2013). Additionally, the recent methodology developed by Garcia-Benadi et al. (2020) has been used to classify the different hydrometeor types of selected case studies.

3.4. Variables evaluated

In rainfall microphysics, the Drop Size Distribution (DSD) has been described by a gamma function (Rosenfeld and Ulrich, 2003; Tokay and Short, 1996; Ulrich and Atlas, 1998). However, a normalized version of this function has been suggested to minimize the correlation between the function parameters (Bringi et al., 2003; Cao and Zhang, 2009; Testud et al., 2001; Willis, 1984):

$$N(D) = N_w f(\mu) \left(\frac{D}{D_m} \right)^\mu \exp \left(- (4 + \mu) \left(\frac{D}{D_m} \right) \right), \quad (1)$$

where $N(D)$ is the raindrop concentration per unit volume ($\text{m}^{-3} \text{ mm}^{-1}$), D is the raindrop diameter (mm), $f(\mu)$ is defined as

$$f(\mu) = \frac{6}{4^4} \frac{(4 + \mu)^{\mu+4}}{\Gamma(\mu + 4)}, \quad (2)$$

and it is function of the shape parameter (μ) and the gamma function (Γ),

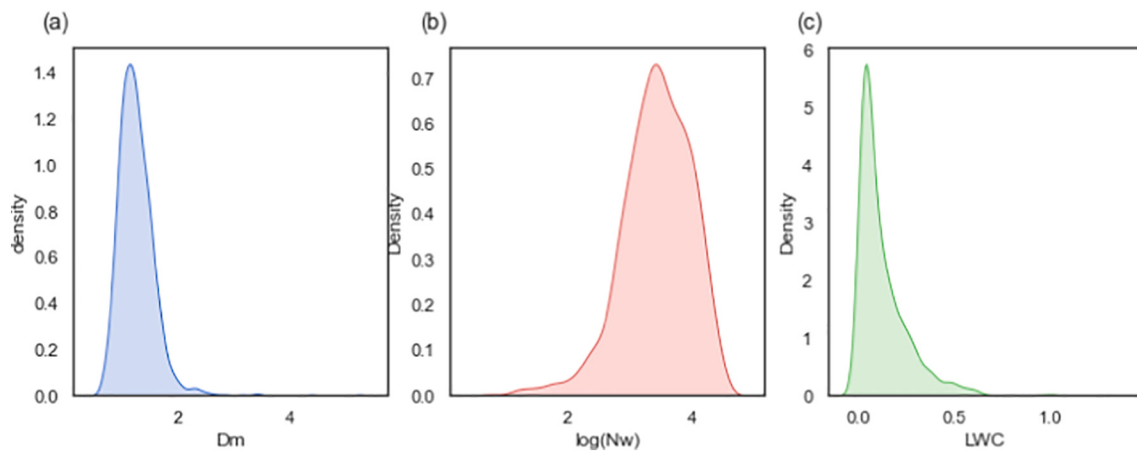


Fig. 4. Kernel Density Estimate of (a) D_m (mm), (b) $\log(N_w)$ (dimensionless) and (c) LWC (g m^{-3}) of rainfall measured by Parsivel during the C2017.

Table 3
Comparison between raindrop size distribution parameter in different published studies.

Paper	Location	Region or area	Precipitation	D_m	$\log(N_w)$	LWC	Observations
<i>This study</i>	Cerdanya valley, Spain	Extratropical inner valley	Total winter	1.17	3.64	0.09	
Casanovas et al., 2021	Sierras de Cordoba, Argentina	Extratropical continental mountain slope and plain	Mountain summer	1.55	3.19	0.14	
			Transition summer	1.69	3.09	0.17	
			Plain summer	1.79	3.02	0.19	
Das et al., 2017	Western Gaths	Tropical mountain slope	Mixed Convective - Stratiform	1.5	–	0.58	
			Stratiform	1.3	–	0.21	
			Convective	1.8	–	1.34	
			Shallow	1.1	–	0.24	
Dolan et al., 2018	Various places	Global	Total annual	1.13	3.95	0.23	Evaluates DO instead of D_m
		High latitudes		1.00	4.12	–	
		Mid latitudes		1.18	3.79	–	
		Low latitudes		1.18	3.94	–	
Hachani et al., 2017	Cévennes-Vivarais region, France	Extratropical mountain slope and plain	Total annual	~1.1	~3.95	–	Median values
Ji et al., 2019	Beijing, China	Extratropical plain near mountain	Stratiform	1.03	3.57	0.08	
			Convective	2.05	3.61	1.08	
Martner et al., 2008	California, USA	Extratropical coastal mountain slope	BB winter	1.25–1.27	3.62–3.75	0.21–0.29	BB = Bright Band
			NBB winter	0.73–0.77	3.89–4.03	0.22–0.31	NBB = Non Bright Band
Seidel et al., 2019	Cuenca, Ecuador	Tropical inner valley	Stratiform	1.07	3.46	–	
	Huaraz, Perú	Tropical inner valley	Convective	1.66	3.76	–	
Suh et al., 2021	Southern South Korea	Extratropical coast	Stratiform	0.93	3.74	–	
Villalobos-Puma et al., 2020	Mantaro basin, Perú	Tropical inner valley	Convective	1.21	4.69	–	
Wen et al., 2016	Jiangning, China	Extratropical plain	Stratiform	0.96–1.09	3.68–4.02	–	
			Convective	1.47–1.58	3.83–3.97	–	
			Stratiform	1.04	2.88	0.08	
			Convective	2.98	3.73	0.70	
			Total	1.15	4.09	0.49	
			Stratiform	1.16	3.78	0.15	
			Convective	1.41	4.37	1.50	
			Shallow	0.64	4.97	0.21	

N_w is the generalized interception ($\text{m}^{-3} \text{ mm}^{-1}$) defined as

$$N_w = \frac{4^4}{\pi \rho_w} \left(\frac{\text{LWC}}{D_m^4} \right), \quad (3)$$

where ρ_w is the liquid water density (10^6 g m^{-3}), LWC is the liquid water content (g m^{-3}) given by

$$\text{LWC} = 10^{-9} \frac{\pi}{6} \rho_w \int D^3 N(D) dD \quad (4)$$

and D_m is the mean volume of drops (mm) defined as

$$D_m = \frac{M_4}{M_3}, \quad (5)$$

where M_n is the n -th moment of the DSD formulated as $M_n = \int D^n N(D)$

dD .

These three parameters are commonly evaluated in many studies and are used here to compare the microphysical properties of the liquid precipitation during C2017 with a selection of different worldwide studies in Section 4.3. As Dolan et al. (2018) presents their results in terms of median volume of the drops D_0 (mm) instead of D_m , we also calculated this variable:

$$D_0 = \frac{3.67 + \mu}{4 + \mu} D_m. \quad (6)$$

Finally, we calculated two more parameters: the radar reflectivity factor and the rain rate. The radar reflectivity factor (Z ; $\text{mm}^6 \text{ m}^{-3}$) is related with the power of the electromagnetic signal backscattered by the hydrometeors and is defined as

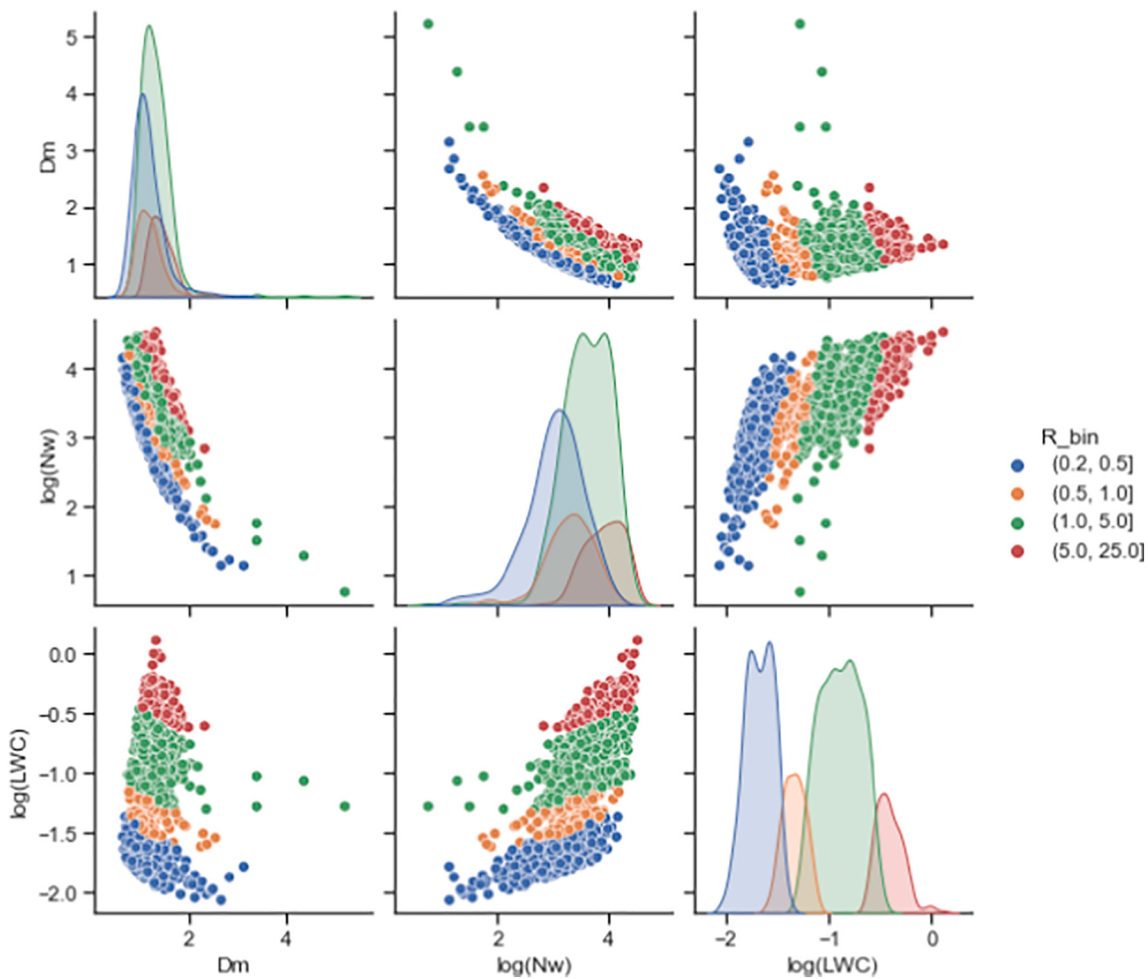


Fig. 5. Kernel Density Estimate (plots in the diagonal) and correlation (remaining plots) between D_m (mm), log(N_w) (dimensionless) and LWC (g m⁻³) for stripped rain rate (mm h⁻¹) of rainfall measured by Parsivel during the C2017.

$$Z = \int D^6 N(D) dD. \quad (7)$$

The Rain Rate (R; mm h⁻¹) is expressed by

$$R = 3.6 \cdot 10^{-3} \frac{\pi}{6} \int v(D) D^3 N(D) dD \quad (8)$$

where $v(D)$ (m s⁻¹) is the fall drop velocity (downward values defined positive) approximated using the empirical equation of [Atlas et al. \(1973\)](#):

$$v(D) = 9.65 - 10.30 \exp(-0.6D) \quad (9)$$

4. Precipitation during C2017

4.1. Characterization of the precipitation events

During the field campaign, precipitation in the area of study ranged from 230 to 962 mm, with lower amounts at valley stations and higher ones at mountain stations ([Fig. 1](#)). Note that precipitation at LECD (260.9 mm, 1097 m asl) is less than half the amount recorded at Malniu (606.7 mm, 2230 m asl), exhibiting the usual precipitation-shadow pattern observed in the area. As usual in winter, many cyclonic systems crossed the region producing most of the precipitation during C2017. This produced a mean flow from the northwest ([Fig. 1a](#)), perpendicular to the mountain systems that enclose the valley.

Different winter precipitation events were intensively observed

during C2017. We define here precipitation event as a period with similar precipitation characteristics and related with the same synoptic structure (e.g. frontal passage) and spaced by at least 3 h without precipitation with another event. Note that during the event the precipitation can be continuous or discontinuous. According to this definition, 42 precipitation events were observed and analysed using the data obtained with the MRR, which operated during all the campaign, and with the Parsivel, when it was available. Ceilometer, microwave radiometer (MWR) and AWSs measurements were used also to support the analysis of the different events. The ceilometer and the MWR were used to retrieve the cloud base and the top of melting layer height, respectively. These instruments have limitations under heavy precipitation conditions ([Costa-Surós et al., 2013](#); [Knupp et al., 2009](#)) but most precipitation rate during C-2017 was weak or moderate. [Table 1](#) shows a brief description of the events occurred during the campaign.

Events were classified by the type of ground precipitation (rain, snow, mixed) and also virga, recorded at LECD aerodrome (1097 m asl). The classification was performed using the MRR profiles and Parsivel information, in particular the automatic WMO SYNOP Present Weather precipitation classification provided by the disdrometer ([OTT, 2016](#); Appendix D). When Parsivel was unavailable, ground precipitation type was estimated using temperature and humidity observations from the LECD AWS, similarly as described in [Casellas et al. \(2021\)](#). Most of the precipitation events included mixed precipitation or transition between rain and snow. Six events were classified as only snow events, and fifteen events were classified as only rain events. When reflectivity values showed precipitation above the ground but zero in the MRR bottom bins

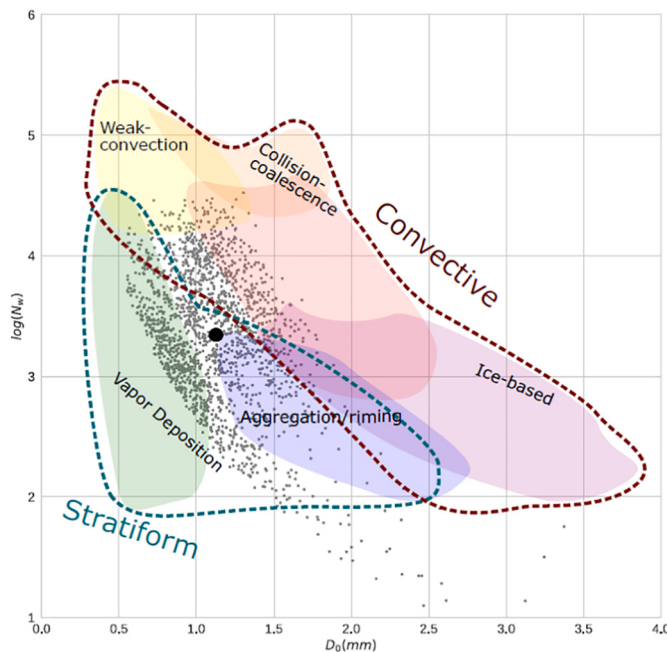


Fig. 6. Distribution of the raindrop size distribution measurements during the C2017 campaign in the D_0 - $\log(N_w)$ space overlapped to Dolan et al. (2018) dominant precipitation processes and convective and stratiform rainfall regimes. The average value of D_0 and $\log(N_w)$ during C2017 is marked with a black dot.

the event was classified as a virga; there were six events with this feature. Only snowfall episodes took place in January and February while only rainfall episodes occurred from February to April, prevailing at the end of the campaign. Transition events were frequent during all the campaign, including late snow periods at the end of the campaign (event #41). These late events with transition features were characterized by frontal passages which strongly modify low level temperature.

Most events showed discontinuous precipitation considering 1-min temporal resolution. Only seven events displayed continuous precipitation and most of these occurred on January. There are also differences between the beginning and the end of the campaign according to depth of the precipitating clouds. In January and early February, precipitating columns tended to be shallow with tops below 2500 m above ground level (*agl*). Instead, in April deep precipitating columns dominated with tops above the 3000 m *agl* that the MRR could measure during C2017.

4.2. Vertical structure of solid precipitation

To investigate the vertical structure of the precipitation over the inner valley, a statistical analysis of reflectivity, spectral width and

Doppler velocity has been conducted. The phase transition of the hydrometeors during rainfall and transition events that occurs at the melting layer aloft does not allow to systematically observe the vertical structure of the measured variables during the winter campaign. To prevent the inhomogeneity of the hydrometeors and their impact on the profile analysis we used only the measures during snowfall events. This ensures that changes observed are due only to changes in microphysical processes and mesoscale or microscale circulations in the inner valley.

Fig. 2 shows the averaged vertical structure of the precipitation during snow events in the C2017 campaign. Similar plots were produced for the whole campaign for rain, mixed and virga events (see Fig. S1 in the Supplementary Information). Reflectivity is related with both quantity and size of the hydrometeors. A downward increase in the reflectivity profile typically indicates snow particles growth. Doppler velocity measures the hydrometeor vertical motions. Snowflakes have a low terminal velocity, of around 1 m s^{-1} , and allow to trace the vertical movement of the air using the Doppler velocity measured by radar profilers such as MRR or similar instruments (Geerts et al., 2011; Gonzalez et al., 2019; Toloui et al., 2014). Similarly, the spectral width associated with solid precipitation particles gives an indication of the turbulence of the air.

Fig. 2a shows that measured reflectivity at 3000 m *agl* during snow events is comprised between -5 and 10 dBZ , averaging 3 dBZ . Reflectivity increases downward until it reaches the height of the mountains, or the crest level, around 1900 m *agl*. Below, reflectivity remains almost constant with values comprised between -5 and 25 dBZ , averaging 10 dBZ . Fig. 2b shows low values of spectral width, between 0.2 and 0.7 m s^{-1} above 2500 m *agl* and averaging 0.3 m s^{-1} . Between 2500 and 700 m *agl* it is noticeable a layer with greater values of spectral width, averaging 0.7 m s^{-1} between 1100 and 1600 m *agl*. However, this layer presents high variability with values ranging between 0.3 and reaching up to 1.6 m s^{-1} in the most extreme cases. Below 700 m *agl*, spectral width decreases averaging 0.5 m s^{-1} with maximum values of 1 m s^{-1} at the lowest bin. Doppler velocity of the hydrometeors (Fig. 3c) may be both upward (negative values) or downward (positive values) up to $\pm 2 \text{ ms}^{-1}$ above the mountain crest level, averaging 0 m s^{-1} above 2600 m *agl*. Doppler velocity steadily increases below averaging downward velocities of 1 m s^{-1} in the last 1300 m.

The statistical analysis of the vertical profile of the snowfall events over the Cerdanya valley shows the general pattern of the microphysical processes and small-scale circulations that occur in this area during the C2017. Snow crystals generally emerge and grow above the crest mountain level. Those crystals are affected by vertical air currents, which can be either upward or downward. Below the mountain peaks at 1900 m *agl*, crystals have grown to full size and downward velocities start to dominate. It is remarkable the structure that generates an increase of the turbulence below the mountain crest level. This structure has been identified in previous studies as a shear layer on windward slopes (Medina et al., 2005). In inner mountains, it decouples the stalled air of the valley and the air of the free atmosphere above the mountains

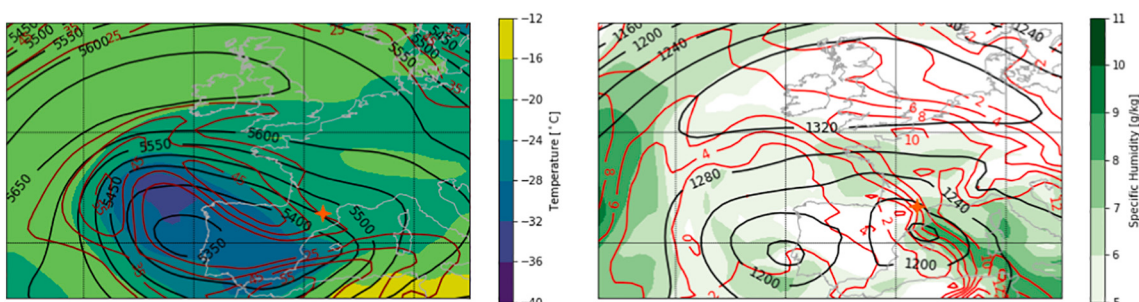


Fig. 7. Synoptic setting on 25 March 2017 at 00:00 UTC. (a) Geopotential height (black lines, mgp) and temperature (shaded) at 500 hPa, and wind speed at 300 hPa (red lines, m s^{-1}). (b) Geopotential height (black lines, mgp), temperature (red lines, $^{\circ}\text{C}$) and specific humidity (shaded) at 850 hPa. Red star indicate the location of LECD aerodrome. (For interpretation of the references to colour in this figure legend, the reader is referred to the web version of this article.)

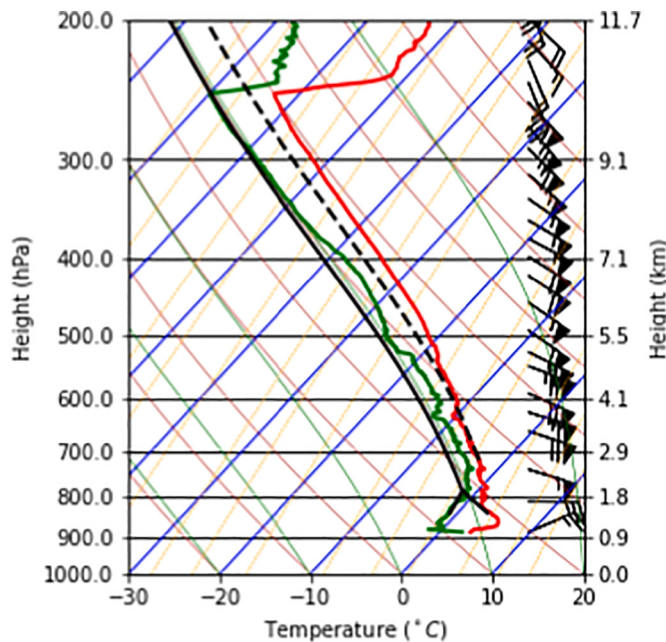


Fig. 8. Sounding launched at LECD on 24 March 2017 at 22:34 UTC showing air temperature (red line), dew point (green line), vertical evolution of an averaged air parcel with the features of the first 100 m (black continuous line) and vertical evolution of an air parcel starting from the convective condensation level (black dashed line). (For interpretation of the references to colour in this figure legend, the reader is referred to the web version of this article.)

(Gonzalez et al., 2019). The air of the free atmosphere above crest level flows according the synoptic setting at mid-levels. Instead, stalled air of the valley bottom can only flow along the basin main axis as suggested by the wind direction measured at LECD AWS during the snow events (Fig. S2). Notice that the main wind direction at LECD flows from a very different direction than climatological wind at 850 hPa (Fig. 1a). Increase of spectral width in the shear layer is not linked with an increase of the reflectivity at the same level, suggesting that, unlike other observations of winter precipitation over mountainous areas (Aikins et al., 2016), turbulence generated by the shear layer does not favour snowfall growth. The steady increase of downward Doppler velocity may indicate an increase of riming below the mountain crest level. Alternatively, it might also be related with the absence of the vertical currents into the stalled valley air.

4.3. Raindrop size distributions

Raindrop size distribution have also been investigated during C2017. To examine the ground level microphysical properties of the liquid precipitation during the campaign, we considered all data classified as rainfall by Parsivel processing. Selected examples of DSDs during the campaign are shown in Fig. 3 showing the diversity of DSDs observed during the campaign: some events present larger tails than others, indicating the presence of larger hydrometeors (e.g. 25 March cold front vs. 30 April postfrontal). Other events present a larger concentration of hydrometeors for all diameters suggesting a convective character of the rainfall event (e.g. 20 April frontal). On the contrary, events with low values of mid to large hydrometeors indicate light stratiform rain or drizzle (eg. 30 April prefrontal and postfrontal). Those events are further discussed in Section 5.

Table 2 shows the mean values, the standard deviation and some percentiles for different parameters of the DSD and Fig. 4 shows the distribution of D_m , $\log(N_w)$ and LWC. Despite they present asymmetric distributions, the mean values of D_m and $\log(N_w)$ are relatively similar to the median values, unlike LWC, which are much more different. We

compared the mean values with a selection of different worldwide studies (Table 3) described in the following subsections.

4.3.1. Properties of the D_m

The mean D_m during C2017 was 1.17 mm with an interquartile range between 0.94 and 1.35 mm. Values of D_m are characteristic of the average precipitation in mid-latitudes (Dolan et al., 2018). Those values are similar to stratiform precipitation in extratropics both in mountain and in plain or coastal areas where reported values in the literature examined range from 0.96 to 1.16 mm (Hachani et al., 2017; Ji et al., 2019; Suh et al., 2021; Wen et al., 2016). Martner et al. (2008), who studied winter precipitation in mountain coastal areas of California distinguishing between Bright Band (BB) and Non-Bright Band (NBB) cases, reported values of 1.25–1.27 mm and 0.73–0.77 mm for BB and NBB cases, respectively. Those results differ substantially from the others reported in extratropical areas.

In the tropics, stratiform precipitation presents a larger D_m (1.3 mm) in tropical mountain slopes of India (Das et al., 2017), but in inner valleys of the Andean mountains values are enclosed between 0.93 and 1.07 mm, similar than in mid-latitudes (Seidel et al., 2019; Villalobos-Puma et al., 2020). Indeed, total precipitation in low latitudes present similar mean D_m than mid-latitudes (Dolan et al., 2018).

Convective precipitation presents larger values of D_m over 1.5 mm (see for example Casanovas et al., 2021; Das et al., 2017; Suh et al., 2021; Villalobos-Puma et al., 2020). However, convective precipitation usually accounts for a small fraction of total occurrence of precipitation in mid-latitudes (although not precipitation depth), having a small impact in the averaged diameter of the total precipitation.

4.3.2. Properties of the $\log(N_w)$

Mean value of $\log(N_w)$ during C2017 was 3.64 with an interquartile range of 3.01 and 3.76. This is slightly below the values obtained by Dolan et al. (2018) for precipitation in mid-latitudes (3.79). It is also similar to other observations of stratiform precipitation in different regions at low-latitudes and mid-latitudes such as 3.46 and 3.74 at Central Andes (Seidel et al., 2019), 3.74 in East China (Wen et al., 2016), 3.53 in Northern China (Ji et al., 2019) and 3.62 in coastal California for BB winter precipitation (Martner et al., 2008). The latter study is relevant as NBB precipitation presents higher values of $\log(N_w)$ associated with orographically forced condensation-coalescence processes in shallow clouds (Martner et al., 2008). Convective and shallow clouds, including NBB precipitation, presents greater $\log(N_w)$, often higher than 4.00 near mountains, except in some extratropical sites where convective precipitation is related to ice-based processes (Casanovas et al., 2021).

4.3.3. Properties of the LWC

Averaged LWC was 0.090 g m^{-3} with an interquartile range of 0.012 and 0.125 g m^{-3} , with a substantial difference between the average and median values, due to the high asymmetry of the LWC distribution (Fig. 4). LWC values found are far below the world wide mean (0.23 g m^{-3}) calculated by Dolan et al. (2018) and below measures with maritime influence; for example, $0.21\text{--}0.29 \text{ g m}^{-3}$ by Martner et al. (2008) for BB winter precipitation in California coastal mountains, 0.21 g m^{-3} by (Konwar et al., 2014) for stratiform precipitation in Western Gaths in India and 0.15 g m^{-3} by Wen et al. (2016) for precipitation in East China. Convective precipitation on those places presents much higher values, over 0.5 g m^{-3} . Instead, mean LWC during C2017 is similar to the 0.08 g m^{-3} measured in Beijing by Ji et al. (2019) and in the Mantaro basin (Perú) by Villalobos-Puma et al. (2020). This reflects the continental characteristics of the Cerdanya valley that despite being relatively near to the sea (i.e. it is closer than Jiangning in Wen et al.) is well isolated by the surrounding mountains.

4.3.4. Inner valley characteristics

The previous results suggest that C2017 winter rainfall was dominated by stratiform precipitation. The absence of a very large quantity of

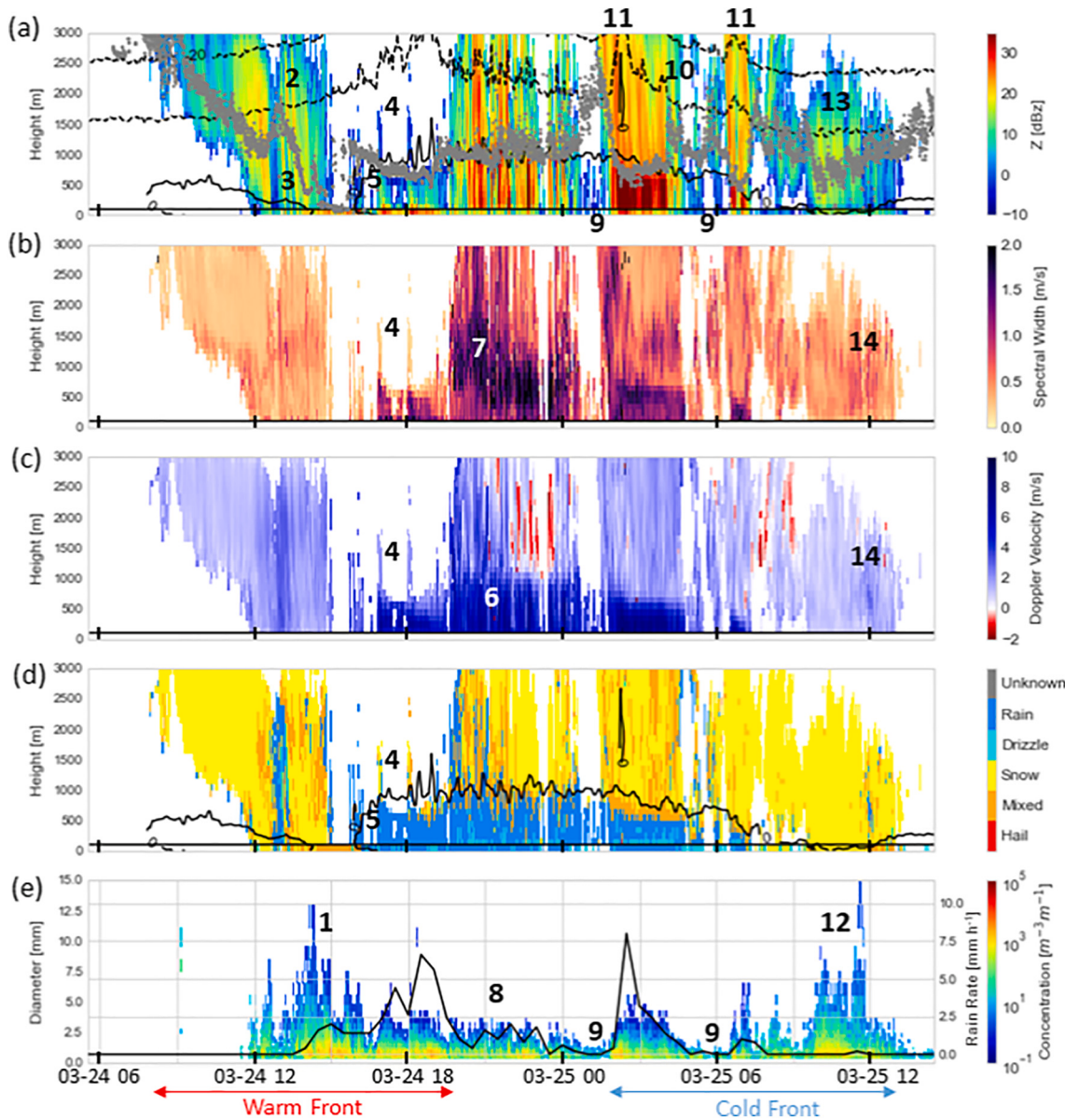


Fig. 9. Time series of the 24–25 March case study. (a) Radar reflectivity from MRR (above black horizontal line) and Parsivel (below black horizontal line). (b) Spectral Width from MRR. (c) Particle Doppler fall velocity from MRR. (d) Type of precipitation derived from MRR (above black horizontal line) and Parsivel (below black horizontal line). (e) Parsivel particle concentration as a function of the widest hydrometeor diameter and rain rate recorded by the LECD AWS. Dotted black lines and grey points in (a) indicate isotherm levels derived from MWR and cloud base height derived from ceilometer, respectively. Black line in (d) indicates the MRR derived zero degrees isotherm. Numeric labels are text references.

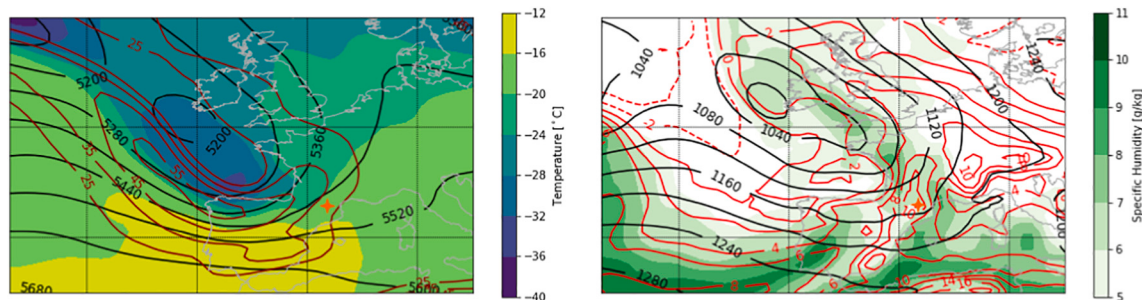


Fig. 10. As in Fig. 7 but for 30 April 2017 at 12:00 UTC.

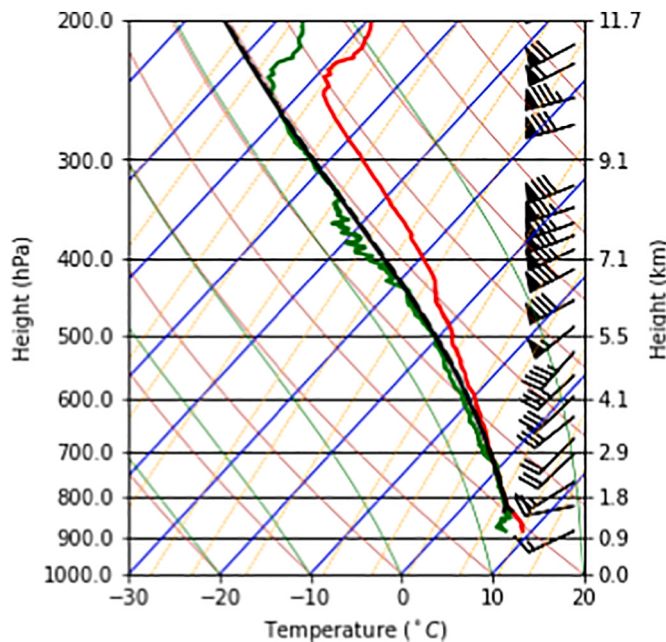


Fig. 11. As in Fig. 8 but for 30 April 2017 at 18:09 UTC.

very small raindrops indicates that shallow convection and coalescence processes do not dominate the winter precipitation of the valley (Martner et al., 2008). Instead, water vapour deposition and stratiform cold-ice processes are likely playing a major role. However, disdrometric characteristics measured during C2017 presented a large variability, indicating that not all precipitation was stratiform. Indeed Table 1 lists a few spring convection events in April (events #34, #35, #36 and #37).

Fig. 5 shows the relation between D_m , N_w and LWC grouped by rain rate computed with Parsivel. As rain rate increases, mean values of D_m , N_w and LWC also increase. However, distributions are overlapped for N_w and especially D_m . As stated in other studies (e.g. Bringi et al., 2003; Dolan et al., 2018), D_m -log(LWC) and log(N_w)-log(LWC) linear correlations are positive, and D_m -log(N_w) correlation is negative. However, the distribution of the parameters in the winter campaign is more similar to those in high-latitudes than those in mid-latitudes as evidenced by the near absence of measures of D_0 over 2 mm reported by Dolan et al. (2018).

To contextualize the measures obtained during C2017 we have represented in Fig. 6 all records on the D_0 -log(N_w) space overlaid with the diagram made by Dolan et al. (2018) showing dominant precipitation mechanisms derived from their principal component analysis of global data (their Fig. 12). Note that most measures are located in the stratiform section of the plot, which is consistent with the disdrometric parameter values discussed at the beginning of this section. Fig. 6 suggests that the predominant rainfall regime during C2017 was stratiform precipitation, highly influenced by vapour deposition and aggregation and riming processes, but some convective events were also present. The later do not exhibit neither the characteristics of typical summer deep convection (ice-based processes) nor those of warm and weak convection (collision-coalescence processes). Instead, they are associated with moderate convection resulting in modest drop sizes of about 1 mm and moderate values of log(N_w) around 4.

5. Vertical structure of precipitation in selected case studies

Previous section showed the general features of precipitation during the campaign. However, these features change with from event to event and sometimes even within the same precipitation event. To illustrate inter-event variability, we selected two different cases of well-observed storms during the C2017 (with all the instruments available). A

particularly interesting case of heavy snowfall was already investigated by Gonzalez et al. (2019), illustrating how precipitation profiles and disdrometric measurements of snow were decoupled from the mountain induced circulations despite the increased turbulence caused by an atmospheric rotor during a mountain wave event. They suggested that conditions that induce the decoupling are caused by low liquid water content and lack of dendritic form, that reduced both riming and aggregation. Here, we present a case with transition from snow to rain occurred between 24 and 25 March 2017, exhibiting an interesting sequence of different hydrometeors. This event was also studied by Soula et al. (2021), but focused in the analysis of winter thunderstorms during C2017. The second case analysed, which occurred at the end of the campaign on 30 April 2017, shows an early spring transition event with scattered liquid precipitation.

5.1. Case of 24–25 March 2017

5.1.1. Synoptic setting and vertical structure of the atmosphere

This case was characterized by a cut-off low located west to the Iberian Peninsula with a 500 hPa cold core of -33°C at 12:00 UTC on 24 March. The interaction between the trough of the cut-off low and the Atlas Mountains produced a secondary low over the Mediterranean Sea north of Algeria that headed north to Catalonia (García-Moya et al., 1989). As the low advanced to our area of study, the system established a backward warm front that crossed the Cerdanya from the northeast and a warm and a moist flux that impinged to the Pyrenees from the southeast (Fig. 7). The two vortex systems whirled in a merry-go-round system producing a Fujiwhara effect (Fujiwhara, 1921). At the end of the day, a well-organized storm in a coma shape and isolated of the main low could be appreciated in the satellite images (Fig. S3). Finally, on 25 March at 12:00 UTC, cold front of the vortex crossed the Pyrenees.

One sounding was launched on 24 March at 22:34 UTC, coinciding with the moment of the strongest flux after the crossing of the warm front (Fig. 8 and S4). The temperature profile shows a single and homogeneous layer with conditional unstable stratification close to the surface up to 10 km *asl*. Moisture is high, especially below 4000 m *asl*. Wind is also strong and homogeneous in both direction and velocity, with around 30 m s^{-1} from the ESE over the 2000 m *asl*.

5.1.2. Microphysical and mesoscale evolution

Fig. 9 shows the evolution of the vertical structure of the low-level precipitation at the Cerdanya valley. The first stage of the event, from 9:00 to 17:00 UTC on 24 March was characterized by the arrival of cloud structures associated to the warm front. This arrival was observed by the ceilometer and the MRR as a progressive decrease of the cloud base and the onset of precipitation nearby the ground. Precipitation was observed as virga before 12:00 UTC and by the Parsivel as snow from 12:00 to 17:00 UTC. Effective reflectivity measured by Parsivel increased at 15:00 UTC when large precipitation particles were observed, probably snow aggregates (see label 1 in Fig. 9). A progressive increase of the temperature over 1000 m *agl* was observed from 10:00 UTC by the MWR (label 2). However, it is noticeable the decrease of the temperature at low levels at the same time (label 3). We hypothesize that the low-level cooling occurred due to the latent heat absorbed during the sublimation process of the solid precipitation (analysed in detail at Section 5.1.3). The wet snow accumulated over the MRR antenna dish attenuated the signal from 16:00 UTC when vertical profiles became unavailable (label 4). As evidenced by the DSD, precipitation continued first in solid phase and later in liquid phase. Signal was recovered at 20:00 UTC when snow over the antenna melted.

From 17:00 UTC on 24 March to 8:00 UTC on 25 March surface precipitation phase changed to rain and precipitation intensity increased to values over 2.5 mm h^{-1} . This stage initiated with a sudden increase of the low-level temperature at low levels that occurred when the air close to the ground became saturated (label 5). When the MRR signal was recovered, it is observed the increase of the downward Doppler velocity

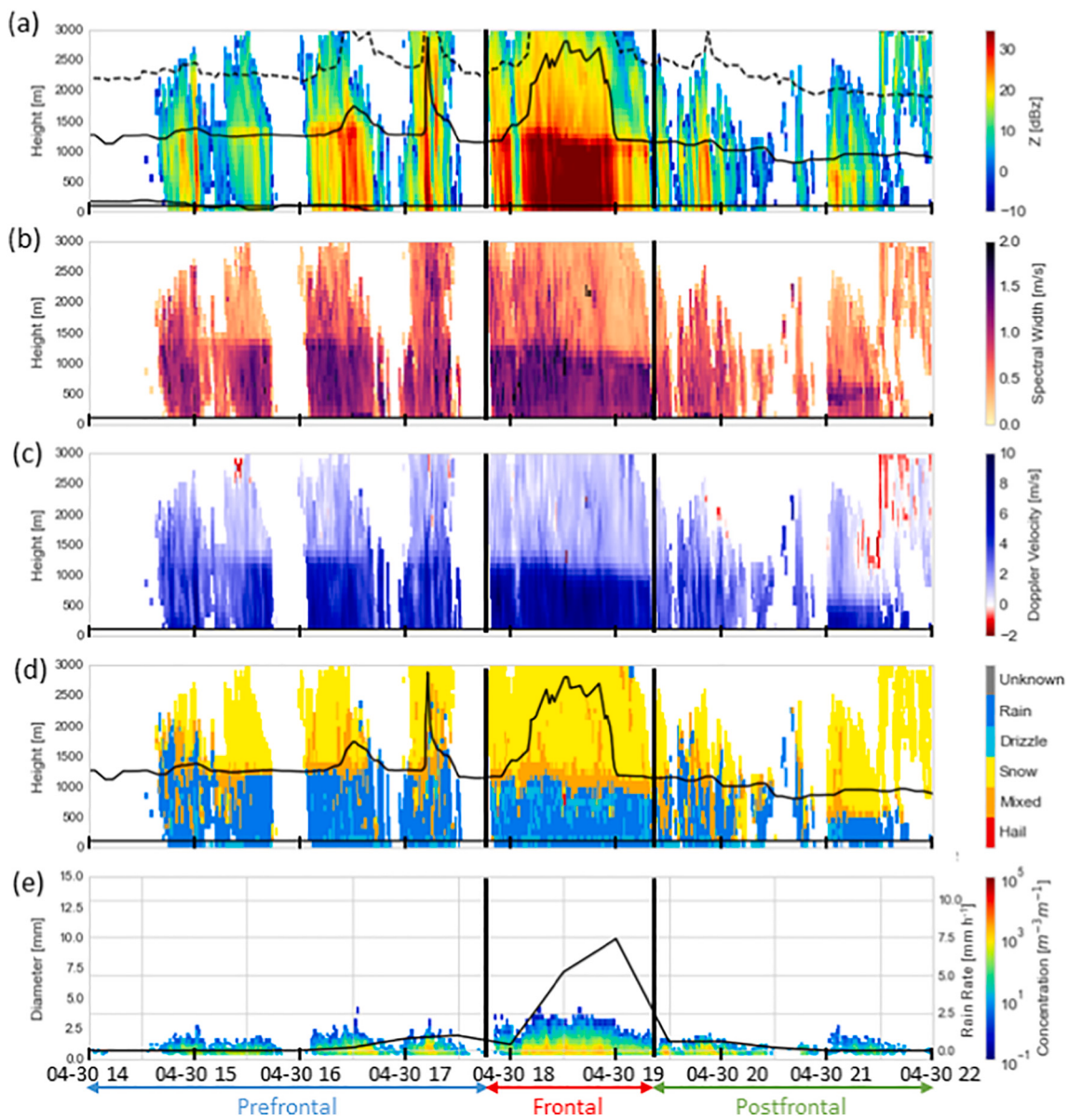


Fig. 12. As in Fig. 9 but for 30 April 2017.

of the precipitation particles as they melt with values over 4 m s^{-1} (label 6). It is noticeable as well, an increase of the spectral width over 2 m s^{-1} during this part of the event (label 7), approximately at the crest level suggesting the influence of a wind shear layer favoured by the decoupling of the stalled air of the valley and the air of the free atmosphere. The increase of the spectral width indicates enhanced turbulence that caused riming on the particles, which favoured the triggering of lightning flashes in the neighbourhood (Soula et al., 2021). DSD of the surface precipitation was homogeneous during this stage; raindrops were generally small, and the bigger ones did not exceed 4 mm (label 8). They decreased during the periods when precipitation was interrupted, probably reaching to the Parsivel only wind-blown small drops from the vicinity (label 9). From 02:00 UTC on 25 March atmospheric temperature steadily decreased indicating the passage of the cold front (label 10). Unlike the warm front, temperature dropped at a similar rate in the whole layer analysed. It can be noticed that the DSD of the rainfall during the cold front is similar to the one in the warm front, with the same D_m and only a small change in N_w , being higher during the warm front (Fig. 3). During this stage it was also observed a characteristic signature of the temperature profiles when the precipitation was

enhanced: the presence of a warm bias of the temperature caused by the emission of the water at similar frequencies used by the MWR (Knupp et al., 2009) (label 11).

At 8:00 UTC on 25 March, precipitation phase changed again over LECD becoming snow. Parsivel measured large particles, probably snow aggregates (label 12). This is consistent with the height of the precipitation growing located between -10 and -20 °C (label 13). Around -15 °C, the conditions for dendritic growth increase (Kobayashi, 1967) and particles are more sensible to aggregating owing to mechanical entanglement (Rauer, 1987). Turbulence decreased during this stage, nonetheless, small areas of increased turbulence concur with greater downward Doppler velocities and increased aggregation (label 14). These areas may correspond to overturning cells with larger mechanical aggregation (Aikins et al., 2016).

5.1.3. Effect of the sublimation during the warm front passage

Here, we study the role of the sublimation on the low-level cooling during the passage of the warm front. As observed at the surface station at LECD, temperature decreased 5.5 °C in 5 h, from 5.3 °C at 11:30 UTC to -0.2 °C at 16:30 UTC (Fig. S5). Similarly, relative humidity increased

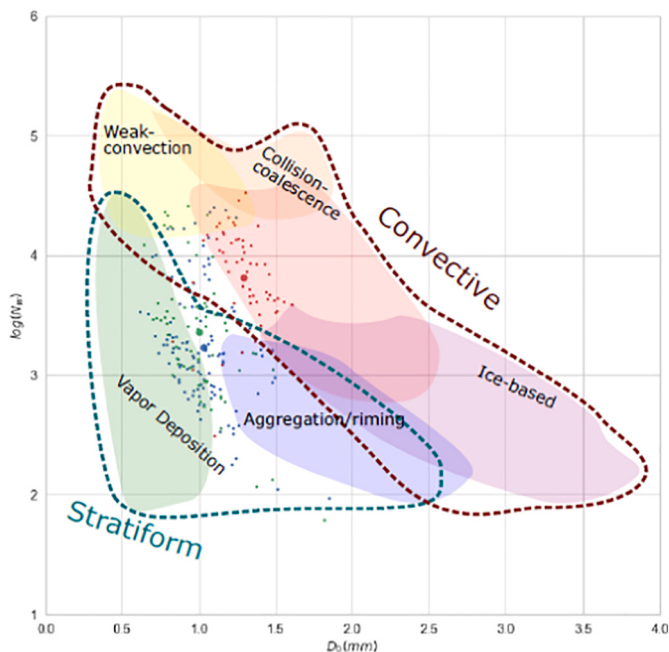


Fig. 13. As in Fig. 6 but for the measurements on 30 April 2017. Blue dots indicate pre-frontal precipitation, red dots indicate frontal precipitation and green dots indicate post-frontal precipitation. Big dots indicate the mean value of each period. (For interpretation of the references to colour in this figure legend, the reader is referred to the web version of this article.)

63% from 36% to 99%, while pressure remained almost constant at around 980 hPa. This corresponds to an increase of 2 g of water vapour per kg of air. Assuming that the increase of the humidity is produced entirely by sublimation of the solid particles falling from aloft, the absorption of latent heat would produce a cooling of 5.6 °C that is compatible with the observations. This process implies that air exchange is suppressed, which is a good assumption in an enclosed inner valley with low ventilation. This is further confirmed by low wind observations recorded at the bottom of the valley.

5.2. Case of 30 April 2017

5.2.1. Synoptic setting and vertical structure of the low troposphere

This event was characterized by a trough over the North Atlantic crossing rapidly from west to east the Iberian Peninsula. Downstream side of the trough with a diffluent pattern was located over our area of study at 12:00 UTC (Fig. 10). A deep surface low associated to the trough deepened south-west to the British Islands. The associated synoptic cold

front crossed the Iberian Peninsula from west to east, reaching to eastern Pyrenees in the afternoon.

Two soundings were launched during this event. The first one was released at 12:05 UTC before the front passage and the second at 18:09 UTC when the front was crossing the area of study. Thermodynamic conditions previous to the front (Fig. S6) showed the presence of a moist and well-mixed layer more than 3000 m deep over the ground. Separated by a stable layer, there was a very dry and almost neutrally stratified layer above. Satellite images showed the presence of trapped lee waves before the front caused by this inversion. In the second sounding inside the front (Fig. 11 and S7), the separation between layers became suppressed. The front, which was modified at low levels by the mountains, produced an important moistening and cooling on the inversion layer. Furthermore, in this layer temperature dropped strongly. However, at low levels the front barely changed the vertical temperature profile, and only increased slightly the stratification stability. Similarly, to the previous case, a single layer with conditional unstable stratification was developed. Wind blew from the WSW at all tropospheric levels, with small shear at low levels but increasing at middle and upper levels.

5.2.2. Microphysical and mesoscale evolution

Fig. 12 shows the evolution of this event. The weather station at LECD (Fig. S8) measured a progressive decrease of the temperature owing to the cold front passage falling 9 °C in 12 h. Over the station the decrease was less pronounced and started later. As previously stated, large increases in MWR temperature (sudden rise of more than 10 °C) are probably due by the emission of raindrops in the reception bands of the MWR (Knupp et al., 2009). Melting layer was well observed, evidenced by a sudden increase of the Doppler velocity and spectral width. It was located around 1200 m agl height until 18:30 and steadily decreased afterwards. This level is close to the crest level, but no clear evidence of a wind shear layer favoured by the decoupling of the air valley and the free atmosphere is found unlike the previous case study.

We divided the event in three stages: prefrontal stage, frontal stage and postfrontal stage. At the prefrontal stage, precipitation started with light and intermittent showers of less than 2 mm h⁻¹. Parsivel measured low surface concentration of small drops of less than 2 mm. As the main frontal band approached, reflectivity increased, and the surface median drop size and concentration increased. The frontal stage, between 18:00 and 19:00 UTC, was the period of highest precipitation intensity that reached 7.5 mm h⁻¹ in 30 min. During this period the reflectivity of the whole column increased, especially below the melting layer, exceeding 35 dBZ. Surface raindrop concentration largely increased and drop particles reached 4 mm. After 19 UTC the precipitation decreased, and the concentration and size of the hydrometeors as well. During the dissipating stage raindrops did not exceed 2 mm diameter. Melting layer height decreased to 700 m. Precipitation continued intermittently until

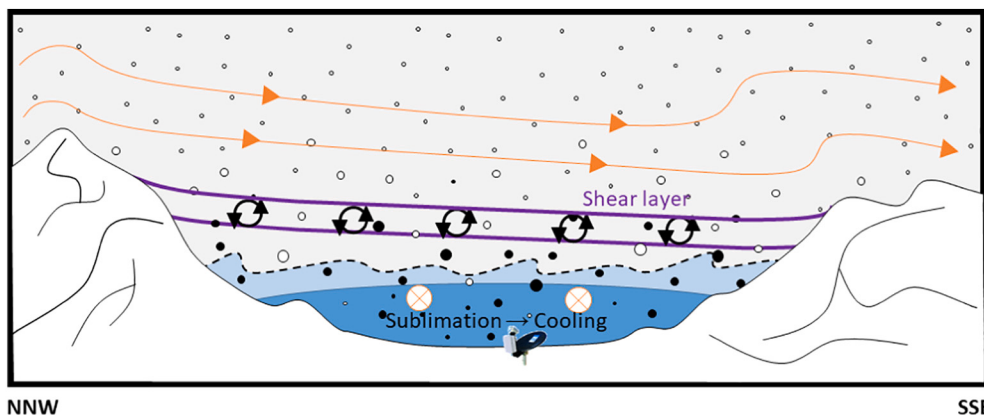


Fig. 14. Conceptual model of winter precipitation in Cerdanya valley from the study of MRR profiles showing the most relevant features: unrimed ice and snow particles (white circles), rimed ice and snow particles (black circles), free atmosphere layers (orange lines), shear layer (purple lines) that decouples the free atmosphere and the stagnant valley air at the valley bottom (dark blue layer) and the cloud base (dashed black line). Around the shear layer turbulence increases, and snow particles grow downward and become rimed by the turbulence. Near the valley floor, snow particles sublimate, cooling the bottom air layer. (For interpretation of the references to colour in this figure legend, the reader is referred to the web version of this article.)

22:00 UTC but virga was observed by MRR afterwards.

Fig. 13 shows the Parsivel measurements during this event into a D_0 -log(N_w) space diagram. During the front passage, D_0 remained in a narrow range of 0.7–1.5 mm. Log(N_w) had a greater variation ranging between 2.5 and 4.5. During the event two main microphysical processes were observed. In the prefrontal and postfrontal stages, stratiform precipitation dominated, especially by vapour deposition process, presenting a similar DSD at both stages (Fig. 3). However, in the frontal stage convective precipitation dominated, with much higher N(D) for all drop diameters (Fig. 3), and although there was no clear dominating process, collision-coalescence may have played a major role. Although precipitation occurred far from the coast, ice-based processes seemed to be suppressed only during the convective period.

6. Concluding remarks

Throughout this article we examined the precipitation data obtained in a wide inner valley of the Pyrenees during the Cerdanya-2017 field campaign. The analysis of the MRR average profiles during the snow events, shows the presence of a persistent shear layer over the valley that decouples the stalled air of the valley and the free atmosphere over the mountains (Gonzalez et al., 2019; Medina et al., 2005). Generally, shear layer increases the turbulence of the air promoting riming of the ice and snow particles as suggested by the patterns observed on average MRR profiles during the campaign. However, occasionally, as in the case studied by Gonzalez et al. (2019), precipitating ice particles may not be affected by riming on these conditions. Other relevant precipitation processes are revealed by the vertical MRR profiles and MWR profiles and the surface data during snow and mixed events such as the cooling effect of the sublimation during the passage of the warm front in the 24 March event. A summary of the effects of the wind shear layer located at crest level and sublimation at the valley bottom upon solid precipitation processes during C2017 is illustrated in a schematic conceptual model shown in Fig. 14.

During the rain periods at the bottom of the valley, our results show that LWC is relatively low compared with other experimental campaigns on mountain environments in similar latitudes, despite its proximity to the Mediterranean Sea. This is probably due to the geographic conditions of the enclosed inner valley, which prevents the advection of moist flows from both Atlantic and Mediterranean. Two principal regimes of rainfall are found during the campaign: (1) stratiform rainfall mainly produced by water vapour deposition processes, although sometimes riming and aggregation become important, and (2) weak convection with slight dominance of collision-coalescence processes. The second one occurs mainly during the frontal passage of 30 April, and during the early spring convective events.

Compared to previous field campaigns devoted to study winter precipitation in mountain areas, the analysis of precipitation events during C2017 contributes to improve our understanding on winter precipitation microphysical processes in an inner valley. The results of this paper suggest that (1) despite being close to the sea, the inner valley favours a cold continental environment and (2) the presence of the wind shear layer may decouple the stalled air of the valley from the free atmosphere inducing turbulent overturning cells that enhances snow growth. Future work could include the comparison of observed vertical precipitation profiles presented and discussed here with those of numerical model prediction systems to assess their capacity in describing the complexities of winter precipitation in inner valleys.

Funding sources

This work was funded by the Spanish Agencia Estatal de Investigación (AEI) and Fondo Europeo al Desarrollo Regional (FEDER) [grant numbers CGL2015-65627-C3-1-R, CGL2015-65627-C3-2-R, CGL2016-81828-REDT, RTI2018-098693-B-C32] the Water Research Institute (IdRA) of the University of Barcelona and the Generalitat de

Catalunya through the ANTALP Research Group [grant number 2017 SGR 1102].

Declaration of Competing Interest

The authors declare that they have no known competing financial interests or personal relationships that could have appeared to influence the work reported in this paper.

Acknowledgments

The Cerdanya-2017 field campaign is a research effort organized by the University of the Balearic Islands, the University of Barcelona. We want to acknowledge the three anonymous reviewers, which through their comments helped to substantially improve the final form of this manuscript.

Appendix A. Supplementary data

Supplementary data to this article can be found online at <https://doi.org/10.1016/j.atmosres.2021.105826>.

References

- Aikins, J., Friedrich, K., Geerts, B., Pokharel, B., 2016. Role of a cross-barrier jet and turbulence on winter orographic snowfall. *Mon. Weather Rev.* 144, 3277–3300. <https://doi.org/10.1175/MWR-D-16-0025.1>.
- Arulraj, M., Barros, A.P., 2021. Automatic detection and classification of low-level orographic precipitation processes from space-borne radars using machine learning. *Remote Sens. Environ.* 257, 112355. <https://doi.org/10.1016/j.rse.2021.112355>.
- Atlas, D., Srivastava, R.C., Sekhon, R.S., 1973. Doppler radar characteristics of precipitation at vertical incidence. *Rev. Geophys.* 11, 1–35. <https://doi.org/10.1029/RG011i001p00001>.
- Bech, J., Codina, B., Lorente, J., Bebbington, D., 2003. The sensitivity of single polarization weather radar beam blockage correction to variability in the vertical refractivity gradient. *J. Atmos. Ocean. Technol.* 20, 845–855. [https://doi.org/10.1175/1520-0426\(2003\)020<0845:TSOSPW>2.0.CO;2](https://doi.org/10.1175/1520-0426(2003)020<0845:TSOSPW>2.0.CO;2).
- Bech, J., Gjertsen, U., Haase, G., 2007. Modelling weather radar beam propagation and topographical blockage at northern high latitudes. *Q. J. R. Meteorol. Soc.* 133, 1191–1204. <https://doi.org/10.1002/qj.98>.
- Bringi, V.N., Chandrasekar, V., Hubbert, J., Gorgucci, E., Randeu, W.L., Schoenhuber, M., 2003. Raindrop size distribution in different climatic regimes from disdrometer and dual-polarized radar analysis. *J. Atmos. Sci.* 60, 354–365. [https://doi.org/10.1175/1520-0469\(2003\)060<0354:RSIDC>2.0.CO;2](https://doi.org/10.1175/1520-0469(2003)060<0354:RSIDC>2.0.CO;2).
- Buisan, S.T., Saz, M.A., López-Moreno, J.I., 2015. Spatial and temporal variability of winter snow and precipitation days in the western and central Spanish Pyrenees. *Int. J. Climatol.* 35, 259–274. <https://doi.org/10.1002/joc.3978>.
- Buisán, S.T., Earle, M.E., Collado, J.L., Kochendorfer, J., Alastrué, J., Wolff, M., Smith, C. D., López-Moreno, J.I., 2017. Assessment of snowfall accumulation underestimation by tipping bucket gauges in the Spanish operational network. *Atmos. Meas. Tech.* 10, 1079–1091. <https://doi.org/10.5194/amt-10-1079-2017>.
- Cao, Q., Zhang, G., 2009. Errors in estimating raindrop size distribution parameters employing disdrometer and simulated raindrop spectra. *J. Appl. Meteorol. Climatol.* 48, 406–425. <https://doi.org/10.1175/2008JAMC2026.1>.
- Casanovas, C., Salio, P., Galligani, V., Dolan, B., Nesbitt, S.W., 2021. Drop size distribution variability in central Argentina during relampago-cacti. *Remote Sens.* 13, 2026. <https://doi.org/10.3390/rs13112026>.
- Casellas, E., Bech, J., Veciana, R., Pineda, N., Rigo, T., Miró, J.R., Safroni, A., 2021. Surface precipitation phase discrimination in complex terrain. *J. Hydrol.* 592, 125780. <https://doi.org/10.1016/j.jhydrol.2020.125780>.
- Conangla, L., Cuxart, J., Jiménez, M.A., Martínez-Villagrassa, D., Miró, J.R., Tabarelli, D., Zardi, D., 2018. Cold-air pool evolution in a wide Pyrenean valley. *Int. J. Climatol.* 38, 2852–2865. <https://doi.org/10.1002/joc.5467>.
- Costa-Surós, M., Calbó, J., González, J.A., Martín-Vide, J., 2013. Behavior of cloud base height from ceilometer measurements. *Atmos. Res.* 127, 64–76. <https://doi.org/10.1016/j.atmosres.2013.02.005>.
- Das, S.K., Konwar, M., Chakravarty, K., Deshpande, S.M., 2017. Raindrop size distribution of different cloud types over the Western Ghats using simultaneous measurements from Micro-Rain Radar and disdrometer. *Atmos. Res.* 186, 72–82. <https://doi.org/10.1016/j.atmosres.2016.11.003>.
- Dolan, B., Fuchs, B., Rutledge, S.A., Barnes, E.A., Thompson, E.J., 2018. Primary modes of global drop size distributions. *J. Atmos. Sci.* 75, 1453–1476. <https://doi.org/10.1175/JAS-D-17-0242.1>.
- Durán-alarcón, C., Boudevillain, B., Genton, C., Graziali, J., Souverijns, N., Van Lipzig, N.P.M., Gorodetskaya, I., Berne, A., 2018. The vertical structure of precipitation at two stations in East Antarctica derived from micro rain radars. *Cryosph. Discuss.* 1–24. <https://doi.org/10.5194/cd-2018-153>.

- Fujiwhara, S., 1921. The natural tendency towards symmetry of motion and its application as a principle in meteorology. *Q. J. R. Meteorol. Soc.* 47, 287–292. <https://doi.org/10.1002/qj.49704720010>.
- Galmarini, S., Steyn, D.G., Ainslie, B., 2004. The scaling law relating world point-precipitation records to duration. *Int. J. Climatol.* 24, 533–546. <https://doi.org/10.1002/joc.1022>.
- García-Benadi, A., Bech, J., Gonzalez, S., Udina, M., Codina, B., Georgis, J.F., 2020. Precipitation type classification of micro rain radar data using an improved doppler spectral processing methodology. *Remote Sens.* 12, 1–23. <https://doi.org/10.3390/rs12244113>.
- García-Moya, J.A., Jansà, A., Díaz-Pabón, R., Rodríguez, E., 1989. Factor influencing the Algerian sea cyclogenesis. In: WMO TD, 298, pp. 87–94.
- Garvert, M.F., Smull, B., Mass, C., 2007. Multiscale Mountain waves influencing a major orographic precipitation event. *J. Atmos. Sci.* 64, 711–737. <https://doi.org/10.1175/jas3876.1>.
- Geerts, B., Miao, Q., Yang, Y., 2011. Boundary layer turbulence and orographic precipitation growth in cold clouds: evidence from profiling airborne radar data. *J. Atmos. Sci.* 68, 2344–2365. <https://doi.org/10.1175/JAS-D-10-05009.1>.
- Gonzalez, S., Bech, J., 2017. Extreme point rainfall temporal scaling: a long term (1805–2014) regional and seasonal analysis in Spain. *Int. J. Climatol.* 37, 5068–5079. <https://doi.org/10.1002/joc.5144>.
- Gonzalez, S., Bech, J., Udina, M., Codina, B., Paci, A., Trápero, L., 2019. Decoupling between precipitation processes and mountain wave induced circulations observed with a vertically pointing K-band Doppler Radar. *Remote Sens.* 11, 1034. <https://doi.org/10.3390/RS11091034>.
- Gorodetskaya, I.V., Kneifel, S., Maahn, M., Thiery, W., Schwein, J.H., Mangold, A., Crewell, S., Van Lipzig, N.P.M., 2015. Cloud and precipitation properties from ground-based remote-sensing instruments in East Antarctica. *Cryosphere* 9, 285–304. <https://doi.org/10.5194/tc-9-285-2015>.
- Hachani, S., Boudevillain, B., Delrieu, G., Bargaoui, Z., 2017. Drop size distribution climatology in Cévennes-Vivarais region, France. *Atmosphere (Basel)* 8, 233. <https://doi.org/10.3390/atmos8120233>.
- Houze, R.A., 2012. Orographic effects on precipitating clouds. *Rev. Geophys.* 50, RG1001 <https://doi.org/10.1029/2011RG000365>.
- Houze, R.A., McMurdie, L.A., Petersen, W.A., Schwall Er, M.R., Baccus, W., Lundquist, J.D., Mass, C.F., Nijssen, B., Rutledge, S.A., Hudak, D.R., Tanelli, S., Mace, G.G., Poellot, M.R., Lettenmaier, D.P., Zagrodnik, J.P., Rowe, A.K., DeHart, J.C., Madaus, L.E., Barnes, H.C., 2017. The olympic mountains experiment (Olympex). *Bull. Am. Meteorol. Soc.* 98, 2167–2188. <https://doi.org/10.1175/BAMS-D-16-0182.1>.
- Ji, L., Chen, H., Li, L., Chen, B., Xiao, X., Chen, M., Zhang, G., 2019. Raindrop size distributions and rain characteristics observed by a PARISVEL disdrometer in Beijing, Northern China. *Remote Sens.* 11, 1479. <https://doi.org/10.3390/rs11121479>.
- Knupp, K.R., Ware, R., Cimini, D., Vandenbergh, F., Vivekanandan, J., Westwater, E., Coleman, T., Phillips, D., 2009. Ground-based passive microwave profiling during dynamic weather conditions. *J. Atmos. Ocean. Technol.* 26, 1057–1073. <https://doi.org/10.1175/2008JTECHA1150.1>.
- Kobayashi, T., 1967. On the variation of ice crystal habit with temperature. *Phys. Snow Ice* 1, 95–104.
- Kochendorfer, J., Nitu, R., Wolff, M., Mekis, E., Rasmussen, R., Baker, B., Earle, M.E., Reverdin, A., Wong, K., Smith, C.D., Yang, D., Roulet, Y.A., Buisan, S., Laine, T., Lee, G., Aceituno, J.L.C., Alastrué, J., Isaksen, K., Meyers, T., Brækkan, R., Landolt, S., Jachcik, A., Poikonen, A., 2017a. Analysis of single-Alter-shielded and unshielded measurements of mixed and solid precipitation from WMO-SPIKE. *Hydrol. Earth Syst. Sci.* 21, 3525–3542. <https://doi.org/10.5194/hess-21-3525-2017>.
- Kochendorfer, J., Rasmussen, R., Wolff, M., Baker, B., Hall, M.E., Meyers, T., Landolt, S., Jachcik, A., Isaksen, K., Brækkan, R., Leeper, R., 2017b. The quantification and correction of wind-induced precipitation measurement errors. *Hydrol. Earth Syst. Sci.* 21, 1973–1989. <https://doi.org/10.5194/hess-21-1973-2017>.
- Konwar, M., Das, S.K., Deshpande, S.M., Chakravarty, K., Goswami, B.N., 2014. Microphysics of clouds and rain over the Western Ghats. *J. Geophys. Res.* 119, 6140–6159. <https://doi.org/10.1002/2014JD021606>.
- Kumar, S., Del Castillo-Velarde, C., Prado, J.M.V., Rojas, J.L.F., Gutierrez, S.M.C., Alvarez, A.S.M., Martíne-Castro, D., Silva, Y., 2020. Rainfall characteristics in the mantaro basin over tropical andes from a vertically pointed profile rain radar and in-situ field campaign. *Atmosphere (Basel)* 11, 248. <https://doi.org/10.3390/atmos11030248>.
- Lasanta, T., Laguna, M., Vicente-Serrano, S.M., 2007. Do tourism-based ski resorts contribute to the homogeneous development of the Mediterranean mountains? A case study in the Central Spanish Pyrenees. *Tour. Manag.* 28, 1326–1339. <https://doi.org/10.1016/j.tourman.2007.01.003>.
- Lemus-Canovas, M., Lopez-Bustins, J.A., Trápero, L., Martin-Vide, J., 2019. Combining circulation weather types and daily precipitation modelling to derive climatic precipitation regions in the Pyrenees. *Atmos. Res.* 220, 181–193. <https://doi.org/10.1016/j.atmosres.2019.01.018>.
- Löffler-Mang, M., Joss, J., 2000. An optical disdrometer for measuring size and velocity of hydrometeors. *J. Atmos. Ocean. Technol.* 17, 130–139. [https://doi.org/10.1175/1520-0426\(2000\)017<0130:AODFMS>2.0.CO;2](https://doi.org/10.1175/1520-0426(2000)017<0130:AODFMS>2.0.CO;2).
- López-Moreno, J.I., Beguería, S., García-Ruiz, J.M., 2002. Influence of the Yesa reservoir on floods of the Aragón River, central Spanish Pyrenees. *Hydrol. Earth Syst. Sci.* 6, 753–762. <https://doi.org/10.5194/hess-6-753-2002>.
- López-Moreno, J.I., Zabalza, J., Vicente-Serrano, S.M., Revuelto, J., Gilaberte, M., Azorin-Molina, C., Morán-Tejeda, E., García-Ruiz, J.M., Tague, C., 2014. Impact of climate and land use change on water availability and reservoir management: scenarios in the Upper Arago'n River, Spanish Pyrenees. *Sci. Total Environ.* 493, 1222–1231. <https://doi.org/10.1016/j.scitotenv.2013.09.031>.
- Maahn, M., Kollias, P., 2012. Improved Micro Rain Radar snow measurements using Doppler spectra post-processing. *Atmos. Meas. Tech.* 5, 2661–2673. <https://doi.org/10.5194/amt-5-2661-2012>.
- Maahn, M., Burgard, C., Crewell, S., Gorodetskaya, I.V., Kneifel, S., Lhermitte, S., Van Tricht, K., Van Lipzig, N.P.M., 2014. How does the spaceborne radar blind zone affect derived surface snowfall statistics in polar regions? *J. Geophys. Res.* 119, 13,604–13,620. <https://doi.org/10.1002/2014JD022079>.
- Martner, B.E., Yuter, S.E., White, A.B., Matrosov, S.Y., Kingsmill, D.E., Ralph, F.M., 2008. Raindrop size distributions and rain characteristics in California coastal rainfall for periods with and without a radar bright band. *J. Hydrometeorol.* 9, 408–425. <https://doi.org/10.1175/2007JHM924.1>.
- Medina, S., Houze, R.A., 2003. Air motions and precipitation growth in Alpine storms. *Q. J. R. Meteorol. Soc.* 129, 345–371. <https://doi.org/10.1256/qj.02.13>.
- Medina, S., Houze, R.A., 2015. Small-scale precipitation elements in midlatitude cyclones crossing the California Sierra Nevada. *Mon. Weather Rev.* 143, 2842–2870. <https://doi.org/10.1175/MWR-D-14-00124.1>.
- Medina, S., Smull, B.F., Houze, R.A., Steiner, M., 2005. Cross-barrier flow during orographic precipitation events: results from MAP and IMPROVE. *J. Atmos. Sci.* 62, 3580–3598. <https://doi.org/10.1175/JAS3554.1>.
- Minder, J.R., Letcher, T.W., Campbell, L.S., Veals, P.G., Steenburgh, W.J., 2015. The evolution of lake-effect convection during landfall and orographic uplift as observed by profiling radars. *Mon. Weather Rev.* 143, 4422–4442. <https://doi.org/10.1175/MWR-D-15-0117.1>.
- Miró, J.R., Peña, J.C., Pepin, N., Sairouni, A., Aran, M., 2018. Key features of cold-air pool episodes in the northeast of the Iberian Peninsula (Cerdanya, eastern Pyrenees). *Int. J. Climatol.* 38, 1105–1115. <https://doi.org/10.1002/joc.5236>.
- Murata, F., Terao, T., Chakravarty, K., Syiemlih, H.J., Cajee, L., 2020. Characteristics of orographic rain drop-size distribution at Cherrapunji, Northeast India. *Atmosphere (Basel)* 11, 777. <https://doi.org/10.3390/ATMOS11080777>.
- OTT Hydromet GmbH, 2016. Operating Instructions Present Weather Sensor OTT Parsivel 2.
- Pagès, M., Pepin, N., Miró, J.R., 2017. Measurement and modelling of temperature cold pools in the Cerdanya valley (Pyrenees), Spain. *Meteorol. Appl.* 24, 290–302. <https://doi.org/10.1002/met.1630>.
- Pérez-Zanón, N., Sigró, J., Ashcroft, L., 2017. Temperature and precipitation regional climate series over the central Pyrenees during 1910–2013. *Int. J. Climatol.* 37, 1922–1937. <https://doi.org/10.1002/joc.4823>.
- Peters, G., Fischer, B., Münter, H., Clemens, M., Wagner, A., 2005. Profiles of raindrop size distributions as retrieved by Microrain Radars. *J. Appl. Meteorol.* 44, 1930–1949. <https://doi.org/10.1175/JAM2316.1>.
- Prat, O.P., Barros, A.P., 2010. Ground observations to characterize the spatial gradients and vertical structure of orographic precipitation - experiments in the inner region of the Great Smoky Mountains. *J. Hydrol.* 391, 141–156. <https://doi.org/10.1016/j.jhydrol.2010.07.013>.
- Rasmussen, R., Baker, B., Kochendorfer, J., Meyers, T., Landolt, S., Fischer, A.P., Black, J., Thériault, J.M., Kucera, P., Gochis, D., Smith, C., Nitu, R., Hall, M., Ikeda, K., Gutmann, E., 2012. How well are we measuring snow: the NOAA/FAA/NCAR winter precipitation test bed. *Bull. Am. Meteorol. Soc.* 93, 811–829. <https://doi.org/10.1175/BAMS-D-11-00052.1>.
- Rauber, R.M., 1987. Characteristics of cloud ice and precipitation during wintertime storms over the mountains of northern Colorado. *J. Clim. Appl. Meteor.* 26, 488–524. [https://doi.org/10.1175/1520-0450\(1987\)026<0488:COIAP>2.0.CO;2](https://doi.org/10.1175/1520-0450(1987)026<0488:COIAP>2.0.CO;2).
- Raupach, T.H., Berne, A., 2015. Correction of raindrop size distributions measured by Parsivel disdrometers, using a two-dimensional video disdrometer as a reference. *Atmos. Meas. Tech.* 8, 343–365. <https://doi.org/10.5194/amt-8-343-2015>.
- Roe, G.H., 2005. Orographic precipitation. *Annu. Rev. Earth Planet. Sci.* 33, 645–671. <https://doi.org/10.1146/annurev.earth.33.092203.122541>.
- Rosenfeld, D., Ulbrich, C.W., 2003. Cloud microphysical properties, processes, and rainfall estimation opportunities. *Meteorol. Monogr.* 30, 237–258. [https://doi.org/10.1175/0065-9401\(2003\)030<0237:CMPPAR>2.0.CO;2](https://doi.org/10.1175/0065-9401(2003)030<0237:CMPPAR>2.0.CO;2).
- Seidel, J., Trachte, K., Orellana-Alvear, J., Figueroa, R., Célérat, R., Bendix, J., Fernandez, C., Huggel, C., 2019. Precipitation characteristics at two locations in the tropical Andes by means of vertically pointing micro-rain radar observations. *Remote Sens.* 11, 2985. <https://doi.org/10.3390/rs11242985>.
- Soula, S., Pineda, N., Georgis, J.F., Leroy, A., Vanpoucke, I., Montanyà, J., Casellas, E., Gonzalez, S., Bech, J., 2021. On the conditions for winter lightning at the Eagle Nest Tower (2537 m asl) during the Cerdanya-2017 field experiment. *Atmos. Res.* 247, 105208. <https://doi.org/10.1016/j.atmosres.2020.105208>.
- Souverijns, N., Gossart, A., Lhermitte, S., Gorodetskaya, I.V., Kneifel, S., Maahn, M., Bliven, F.L., van Lipzig, N.P.M., 2017. Estimating radar reflectivity - snowfall rate relationships and their uncertainties over Antarctica by combining disdrometer and radar observations. *Atmos. Res.* 196, 211–223. <https://doi.org/10.1016/j.atmosres.2017.06.001>.
- Stark, D., Colle, B.A., Yuter, S.E., 2013. Observed microphysical evolution for two East Coast winter storms and the associated snow bands. *Mon. Weather Rev.* 141, 2037–2057. <https://doi.org/10.1175/MWR-D-12-00276.1>.
- Suh, S.H., Kim, H.J., Lee, D.I., Kim, T.H., 2021. Geographical characteristics of raindrop size distribution in the southern parts of South Korea. *J. Appl. Meteorol. Climatol.* 60, 157–169. <https://doi.org/10.1175/JAMC-D-20-0102.1>.
- Testud, J., Oury, S.P., Black, R.A., Amayenc, P., Dou, X., 2001. The concept of “normalized” distribution to describe raindrop spectra: a tool for cloud physics and cloud remote sensing. *J. Appl. Meteorol.* 40, 1118–1140. [https://doi.org/10.1175/1520-0450\(2001\)040<1118:TCONDT>2.0.CO;2](https://doi.org/10.1175/1520-0450(2001)040<1118:TCONDT>2.0.CO;2).

- Tokay, A., Short, D.A., 1996. Evidence from tropical raindrop spectra of the origin of rain from stratiform versus convective clouds. *J. Appl. Meteorol.* 35, 355–371. [https://doi.org/10.1175/1520-0450\(1996\)035<0355:EFTRSO>2.0.CO;2](https://doi.org/10.1175/1520-0450(1996)035<0355:EFTRSO>2.0.CO;2).
- Toloui, M., Riley, S., Hong, J., Howard, K., Chamorro, L.P., Guala, M., Tucker, J., 2014. Measurement of atmospheric boundary layer based on super-large-scale particle image velocimetry using natural snowfall. *Exp. Fluids* 55, 1737. <https://doi.org/10.1007/s00348-014-1737-1>.
- Trapero, L., Bech, J., Rigo, T., Pineda, N., Forcadell, D., 2009. Uncertainty of precipitation estimates in convective events by the Meteorological Service of Catalonia radar network. *Atmos. Res.* 93, 408–418. <https://doi.org/10.1016/j.atmosres.2009.01.021>.
- Trapero, L., Bech, J., Duffourg, F., Esteban, P., Lorente, J., 2013a. Mesoscale numerical analysis of the historical November 1982 heavy precipitation event over Andorra (Eastern Pyrenees). *Nat. Hazards Earth Syst. Sci.* 13, 2969–2990. <https://doi.org/10.5194/nhess-13-2969-2013>.
- Trapero, L., Bech, J., Lorente, J., 2013b. Numerical modelling of heavy precipitation events over Eastern Pyrenees: analysis of orographic effects. *Atmos. Res.* 123, 368–383. <https://doi.org/10.1016/j.atmosres.2012.09.014>.
- Udina, M., Bech, J., Gonzalez, S., Soler, M.R., Paci, A., Miró, J.R., Trapero, L., Donier, J. M., Douffet, T., Codina, B., Pineda, N., 2020. Multi-sensor observations of an elevated rotor during a mountain wave event in the Eastern Pyrenees. *Atmos. Res.* 234, 104698. <https://doi.org/10.1016/j.atmosres.2019.104698>.
- Ulbrich, C.W., Atlas, D., 1998. Rainfall microphysics and radar properties: analysis methods for drop size spectra. *J. Appl. Meteorol.* 37, 912–923. [https://doi.org/10.1175/1520-0450\(1998\)037<0912:RMARPA>2.0.CO;2](https://doi.org/10.1175/1520-0450(1998)037<0912:RMARPA>2.0.CO;2).
- Villalobos-Puma, E., Martinez-Castro, D., Flores-Rojas, J.L., Saavedra-Huanca, M., Silva-Vidal, Y., 2020. Diurnal cycle of raindrops size distribution in a valley of the peruvian central Andes. *Atmosphere (Basel)* 11, 38. <https://doi.org/10.3390/ATMOS11010038>.
- Wen, L., Zhao, K., Zhang, G., Xue, M., Zhou, B., Liu, S., Chen, X., 2016. Statistical characteristics of raindrop size distributions observed in East China during the asian summer monsoon season using 2-D video disdrometer and micro rain radar data. *J. Geophys. Res.* 121, 2265–2282. <https://doi.org/10.1002/2015JD024160>.
- Wen, L., Zhao, K., Zhang, G., Liu, S., Chen, G., 2017. Impacts of instrument limitations on estimated raindrop size distribution, radar parameters, and model microphysics during mei-yu season in east China. *J. Atmos. Ocean. Technol.* 34, 1021–1037. <https://doi.org/10.1175/JTECH-D-16-0225.1>.
- Willis, P.T., 1984. Functional fits to some observed drop size distributions and parameterization of rain. *J. Atmos. Sci.* 41, 1648–1661. [https://doi.org/10.1175/1520-0469\(1984\)041<1648:FFTSOD>2.0.CO;2](https://doi.org/10.1175/1520-0469(1984)041<1648:FFTSOD>2.0.CO;2).
- WMO, 1994. World Meteorological Organization Guide to Hydrological Practices, 5th ed. (Geneva, Switzerland).
- WMO, 2014. Measurement of precipitation. In: Guide to Meteorological Instruments and Methods of Observation. World Meteorological Organization (WMO), Geneva, Switzerland, pp. 186–221.
- Xercavins, A., 1985. Els climes del Pirineu Oriental: des de les terres gironines fins a la Catalunya Nord i Andorra. *Doc. d'Anàlisi Geogr.* 7, 81–102.